INL/JOU-20-60341-Revision-0

Modified Microstructures in Proton Irradiated Dual Phase 308L Weldment Filler Material

May 2021

Zhen Li, Weicheng Zhang, Benjamin J. Sutton, Gary S. Was, Brent J. Heuser, Xianming Bai, Xun Zhan

Changing the World's Energy Future

INL is a U.S. Department of Energy National Laboratory operated by Battelle Energy Alliance, LLC

INL/JOU-20-60341-Revision-0

Modified Microstructures in Proton Irradiated Dual Phase 308L Weldment Filler Material

Zhen Li, Weicheng Zhang, Benjamin J. Sutton, Gary S. Was, Brent J. Heuser, Xianming Bai, Xun Zhan

May 2021

Idaho National Laboratory
Idaho Falls, Idaho 83415

http://www.inl.gov

Prepared for the
U.S. Department of Energy
Under DOE Idaho Operations Office
Contract DE-AC07-05ID14517

Modified Microstructures in Proton Irradiated Dual Phase 308L Weldment Filler Material

Zhen Li[a*], Xun Zhan[b], Xian-Ming Bai[c,d], Shao-Chun Lee[a], Weicheng Zhong[a], Benjamin J. Sutton[e], and Brent J. Heuser[a*]

[a] Department of Nuclear, Plasma, and Radiological Engineering, University of Illinois, Urbana, IL, 61801, USA.

[b] Department of Materials Science and Engineering, University of Illinois, Urbana, IL, 61801, USA.

[c] Department of Materials Science and Engineering, Virginia Polytechnic Institute and State University, Blacksburg, VA 24061, USA

[d] Computational Mechanics and Materials Department, Idaho National Laboratory, Idaho Falls, ID 83415

[e] Electric Power Research Institute, Charlotte, NC, 28262, USA

Abstract

The effect of proton irradiation on the microstructure of δ ferrite—γ austenite mixed phase 308L filler material in a 508-304 dissimilar metal weldment was investigated over a depth of 0 to 10 μm. Ni-Si-Mn G-phase precipitates were observed with SEM and TEM in δ ferrite but not in γ austenite. Our density functional theory based calculations show that the G/Fe interface energy in δ-Fe is significantly lower than that in γ-Fe (0.35 vs. 1.25 J/m^2), which provides a thermodynamics-based explanation for our experimental observations of preferential formation of G-phase in δ ferrite. STEM-EDS, TEM dark field imaging, and diffraction patterns confirmed the Ni-Si-Mn enriched precipitates were G-phase precipitates with a stoichiometry of $Mn_6Ni_{16}Si_7$. Intragranular voids and Ni-Si enriched clusters were observed in irradiated γ austenite. Additionally, Ni and Si segregation was observed along the void interfaces. In both cases, Ni-Si clusters and segregation to voids, selected area diffraction patterns did not reveal the existence of

a second phase. Proton irradiation induced Cr depletion and Si and Ni enrichment at γ–γ austenite grain boundaries that was characterized with STEM/EDS.

Key words:

SA508-304L DMW, proton irradiation, G-phase precipitation, Ni-Si enriched clustering.

1. Introduction

Low-alloy steel (LAS) SA508 is used in light water nuclear reactor (LWR) power plants as reactor pressure vessel (RPV), pressure vessel nozzles, and in steam generator components. SA508 has sufficient strength to withstand high tensile stress and a high fracture toughness to assure the safe operation in nuclear power plants. In addition, SA508 is not susceptible to stress corrosion cracking (SCC) [1, 2]. As for other commonly used steels in nuclear energy systems such as 300 series stainless steels, the excellent corrosion resistance makes these alloys a good candidates for tubing and piping in the LWR systems [3]. However, 300 series stainless steels are susceptible to SCC [4-6] as well as irradiation-assisted stress corrosion cracking (IASCC) [7, 8].

SA508-304L dissimilar metal welds (DMWs) are common in LWRs. However, the susceptibility of stainless steel weld joint to SCC was reported to be worse compared to base low-alloy steel and stainless steel [9]. Stainless steel 308L has a similar composition to 304L is a common transition weld joint between ferritic and austenitic steels [3]. The percentage of precipitated δ ferrite and the microstructure in 308L filler depends on the elemental composition and the cooling rate after the welding process [10]. In addition, it has been reported that a certain fraction of δ ferrite precipitation in the matrix austenite 308L filler can improve the solidification cracking resistance of 308L weld joint [10].

Two different precipitates, γ' and G phase, have reported in irradiated 300 series γ austenite stainless steels [11-13]. γ' has cubic crystal structure ($Pm\bar{3}m$), formula unit of Ni_3Si, and a lattice parameter of 0.354 nm [14]. Ni-Si enriched clusters with compositions close to γ' have been observed in 300 series austenite stainless steels [15] and are believed to be precursors to the γ' phase [16]. G-phase precipitates, with a formula unit of $M_6Ni_{16}Si_7$ (M=transition metal element), is also a cubic crystal structure with larger lattice parameter compared to γ' [11]. G-phase

precipitation has been reported in δ ferrite of cast stainless steel after neutron irradiation [17]. Mechanical properties have been investigated for irradiated 308L stainless steels [18, 19]; microstructural evolution of the proton irradiated 308L filler has also been reported [20, 21]. However, the different response of δ ferrite and γ austenite to proton irradiation is not well understood. It is therefore important to understand the response of 308L filler under proton irradiation with both advanced micro-characterization techniques and DFT calculations prior to investigate the behavior of IASCC on 308L filler.

In this work, we irradiated the dual phase (δ ferrite and γ austenite) 308L filler with 2 MeV protons at 360 ◦C and to damage level of 5 displacements per atom (dpa). The microstructures of δ ferrite and γ austenite before and after proton irradiation were studied with advanced micro-characterization techniques. Changes to the microstructure and elemental distribution in δ ferrite and γ austenite are reported and the underlying mechanism is interpreted by density functional theory (DFT) calculations.

2. Experimental and computational procedures

2.1 Materials

The composition of the SA508-304L DMW materials studied here are listed in Table 1. This nuclear grade weldment was fabricated by the Electric Power Research Institute. A schematic illustration of the weldment is shown in Figure 1. The Figure 1 inset shows an irradiated TEM bar specimen. This weldment was fabricated using the gas tungsten arc welding (GTAW) technique. A total of 54 bead lines of SS 309L butter were deposited in five layers on SA509 with the interpass temperature of 177 °C. The bevel angle was 60 degrees. The current average, voltage average, average travel speed were 215 A, 9.9 V, and 8.1 cm/min, respectively. A post-weld heat treatment (PWHT) was performed on the SA508 plate with 309L butter at 635 °C ± 10 °C for 1.5 hours. The heat-up and cool-down temperature ramp rate was below 70 °C/hr when the temperature was above 220 °C. The butter was then cut to a thickness of 1.5 cm. The 309L butter was welded to the 304L using 308L filler with bevel angle of 60 degrees. The 308L filler weld consisted of a total of 57 bead lines in 18 layers and the interpass temperature was 177 °C. The fit-up root opening was 0.32 cm and the fit-up width at the joint top was 3.2 cm. The current, voltage, and travel speed of the 308L groove weld were 240 A, 10.4 V, and 9.4 cm/min, respectively. A PWHT was not performed for the 308L groove weld, consistent with industry practice. The 308L filler material recrystallizes upon cooling into a mixed phase microstructure of δ ferrite and γ austenite.

2.2 Experiment Methods

Proton irradiation of TEM bar specimens was performed at the Michigan Ion Beam Laboratory (MIBL). Specimens (such as the Figure 1 inset) were cut from 308L filler and mechanically polished using SiC. Residual surface damage was removed by electropolishing with a 90-10

methanol-perchloric electrolytic solution at -30 °C. A potential of 40 V was applied between the electrolyte and the 308L specimen for 15 s.

A 3 MV National Electronics Corporation Pelletron accelerator in the MIBL was used to generate 2 MeV protons to irradiate the 308L filler specimen. Proton irradiation was performed at 360 °C under a base pressure of 10^{-7} Torr. The total proton current was 30 micro-Amps over a 1.12 cm^2 area. The total irradiation time was 140 hours. The irradiation temperature was set to compensate dose rate difference between neutron (around 300 °C in LWR) and proton irradiation according to Mansur's invariance theory [22]. Simulated damage profiles of the proton irradiation was calculated by Stopping and Range of Ions in Matter (SRIM) [23]. Two-MeV protons have a damage profile with a peak at about 20 μm in 308L. A total irradiation damage level of 5 dpa is achieved in a 140 h irradiation test, corresponding to a damage rate of 9.9×10^{-6} dpa/s. The center of TEM bar b (the specimen presented here) was irradiated over a 2 mm by 10 mm area.

Electron backscatter diffraction (EBSD) was performed with Thermo Scios2 Dual-Beam SEM/FIB, which has a Hikari Super EBSD detector. Specimens for EBSD were mechanically polished with 4000 grit SiC and then vibration polished using 0.05 um Al_2O_3 solution. An EBSD step size of 1 μm was used to have a global picture of the microstructure of 308L filler. In addition, Thermo Scios2 Dual-Beam SEM/FIB was used to acquire SEM images and preparing lift-out TEM specimens. TEM specimens with a dimension of 10 μm by 10 μm were thinned with a Ga ion milling to less than 100 nm, which is a thickness that is transparent to electron beam.

TEM bright field and dark field images and diffraction patterns were taken with a JOEL 2010 Lab6 transmission electron microscope at 200 kV. STEM/STEM-EDS were performed on FEI

Themis Z Advanced Probe Aberration Corrected Analytical TEM/STEM at 300 k with a 4-crystal EDS detection system.

2.3 Density functional theory (DFT) calculations

As described later in this paper, our experimental characterization shows that $Mn_6Ni_{16}Si_7$ based G phase can form in body-centered-cubic (BCC) δ ferrite but not in face-centered-cubic (FCC) γ austenite. To provide a theoretical explanation of our experimental observation, DFT calculations were conducted to calculate the interface energies between the G-phase ($Mn_6Ni_{16}Si_7$) and Fe, where both BCC and FCC Fe are considered. $Mn_6Ni_{16}Si_7$ G-phase has a cubic structure (space group: $Fm\bar{3}m$) and one unit cell contains 116 atoms ($Mn_{24}Ni_{64}Si_{28}$) [24]. The lattice parameter (1.112 nm [24]) is about 4 times of BCC Fe and 3 times of FCC Fe. Therefore, to create a G-phase/Fe_{BCC} interface system, a BCC Fe box of 4×4×4 unit cells (128 Fe atoms) is placed on a G phase unit cell along the [001] direction so that the entire system contains 244 atoms. Similarly, to create a G-phase/Fe_{FCC} interface system, a FCC Fe box of 3×3×3 unit cells (108 Fe atoms) is placed on a G phase unit cell along the [001] direction and the total number of atoms is 224. Since periodic boundary conditions are employed, two interfaces are created in each system. The interface energy is thus calculated as,

$$\sigma_{G/Fe} = \frac{E_{G/Fe} - E_G - E_{Fe}}{2A}, \qquad (2.1)$$

where $E_{G/Fe}$ is the total energy of the interface system, E_G is the energy of a standalone bulk G-phase, E_{Fe} is the energy of a standalone bulk Fe that has the same structure and number of atoms as in the interface system, and A is the interface area.

It is well known that BCC α-Fe is stable at low temperatures and has a ferromagnetic (FM) state below the Curie temperature, FCC γ-Fe is stable at moderate temperatures and has a paramagnetic (PM) state, and BCC δ-Fe is stable at high temperatures. The magnetic state of δ-Fe is likely to be paramagnetic. It is well known that δ-Fe is stable at the high temperature range (>1653 K), which is well above the Curie point of Fe (1043 K). The magnetic state of Fe changes from ferromagnetic to paramagnetic above the Curie point and it is reasonable to assume that δ-Fe is in a PM state. It is possible that δ-Fe has a non-magnetic (NM) state as well. In this work, both non-magnetic (NM) and PM states are considered for δ-Fe to distinguish α-Fe and δ-Fe. For the $Mn_6Ni_{16}Si_7$ G-phase, neutron diffraction experiments [24] show that the magnetic state is complex and temperature dependent, and is dominated by the magnetic moment of Mn. In this work, the $Mn_6Ni_{16}Si_7$ G-phase is treated as FM state, which is the same approach used by King *et al*. [25]. In addition, NM state is also considered for $Mn_6Ni_{16}Si_7$ G-phase to account for the loss of magnetism at high temperatures. Therefore, combinations of different magnetic states between Fe and G-phase are considered for calculating the interface energies, as detailed in the Results Section.

All the DFT calculations are conducted using the Vienna Ab initio Simulation Package (VASP). During structural relaxation of simulation systems, both the simulation cell and shape as well as atom positions are allowed to change. The Projector-Augmented-Wave (PAW) method [26] is used and the plane wave cutoff energy is set to 450 eV. The electron exchange-correlation interactions are modeled under the generalized gradient approximations (GGA) using the standard Perdew–Burke–Ernzerhof (PBE) functionals [27] implemented in the VASP 5.4. Gaussian smearing with a smear width of 0.05 eV is used to set the partial occupancies of orbitals. The energy convergence criterion is 10^{-4} eV in all simulations. In most of the simulations, the force

convergence of 0.01 eV/Å is also used. The spin polarization effect is activated when the magnetic effects are modeled. For FM state, the initial magnetic moment is set to $5\mu_B$ for Fe, and $6\mu_B$ for Mn. To approximate the PM state for both BCC and FCC Fe, the initial magnetic moments of Fe atoms are randomly distributed between $-3\mu_B$ and $3\mu_B$ with a mean value of $0\mu_B$. In all simulations, a 3×3×3 gamma-centered grid is used for k-point mesh.

3. Results

3.1 Microstructure of as-received 308L filler weld joint

3.1.1 EBSD

Two phases, δ ferrite and γ austenite, were seen in the microstructure of the as-received 308L filler shown in Figure 2. The as-received 308L filler material was cut from the same region as the irradiated TEM bar b, indicated in Figure 1. As a precipitate during the cooling process of austenite 308L, δ ferrite, seen as yellow phases in Figure 2a, has the skeletal morphology. δ ferrite has a body centered cubic (BCC) structure and the lattice parameter is 0.290 nm [28]. γ austenite has an face centered cubic (FCC) structure and the lattice parameter is 0.361 nm [29]. The fact that lattice parameter changes as the solutes concentration varies is well known [30, 31]; the lattice parameters of δ ferrite and γ austenite can change as the concentration of alloying elements varies. The size of δ ferrite grains are in the range of tens of micrometers and that of γ austenite grains are in the range of hundreds of micrometers, as indicated in Figure 2b.

3.1.2 TEM

The specimens analyzed here were lifted out from as-received 308 material at a depth of approximate 10 μm. The size of the lifted out TEM specimen is 10 μm by 10 μm. Figure 3 shows the TEM micrographs and selected area diffraction (SAD) patterns of the as-received 308L filler material. Pt is deposited on the free surface to protect the FIB sample as seen in Figure 3a. The dark patterning in both δ ferrite and γ austenite are Bragg diffraction contrast bending and thickness contours. Only one diffraction pattern is observed, along the [113] zone axis in Figure 3b. Based on the Figure 3b SAD pattern, the d-spacing of the (110) plane is 0.200 nm, which agrees well with known the d-spacing (0.202 nm) for the (110) plane in δ ferrite. In addition, a single diffraction pattern is observed in Figure 3c along the [112] zone axis of γ austenite. The measured

d-spacing of (111) plane in Figure 3c is 0.204 nm, which is good agreement with the known d-spacing (0.208 nm) of the (111) plane in γ austenite.

3.2 Microstructure of Irradiated 308 Filler with unirradiated region

3.2.1 SEM

As mentioned earlier, proton irradiation was performed at 360 °C for 140 h. The simulated proton irradiation damage profile shown in Figure 4 and was obtained with the quick Kinchin-Pease option in the Stopping and Range of Ions in Matter (SRIM) software [23]. Figure 4 shows that the differential damage of protons increases gradually in 308L to a depth of approximately 15 μm. SEM images of the unirradiated and irradiated 308L filler material (this is the same TEM bar b shown in Figure 1) are compared in Figure 5. Precipitation was not observed in unirradiated δ ferrite 308L filler, but is clearly seen in the δ-ferrite grains and along the δ/γ phase boundaries of the irradiated portion of TEM bar b (the center 2 mm by 10 mm region was irradiated). Specifically, Figure 5a indicates that in the unirradiated but heat exposed regions, G-phase does not precipitate in δ ferrite. Thus, the thermal aging associated with the 360 °C 140 hour temperature exposure does not induce G-phase precipitation.

3.2.2 TEM

A 10 μm by 10 μm TEM sample was lifted out from the irradiated region of TEM bar b beneath to a depth of approximately 10 μm from the free surface. Figure 6a is a TEM bright field image of the δ ferrite grain along the [001] BCC zone axis and shows precipitates in the irradiated 308L filler region approximately 10 μm beneath the free surface. These precipitates have a diameter approximately 20 nm. The white and black bands within the precipitates in Figure 6a and 6b are Moire fringes, which is a diffraction contrast induced by the overlapping of phases (precipitates and BCC δ ferrite matrix) with different lattice structures. The calculated density of these

precipitates is in the range of 100 per mm^2 based on the bright field image in Figure 6a. Two sets of diffraction patterns are observed in Figure 6a. The δ ferrite zone axis corresponds to BCC [001] and the calculated d-spacing of (020) reflection is 0.142 nm, in agreement with that of δ ferrite. The second set of reflections (one is circled in Figure 6a) corresponds to the precipitates in δ ferrite. In addition, these precipitates show strong contrast in the Figure 6b dark field image.

Figure 7 is a STEM-HAADF image and a series of STEM-EDS images of a lift-out specimen with the upper portion near the free surface. This set of images shows a δ ferrite grain extending downward in the middle of the imaged region. Based on the STEM-EDS maps in Figure 7, the BCC δ ferrite is rich in Cr and poor in Ni. In contrast, FCC γ austenite is rich in Ni, which is an FCC crystal stabilizer. The δ ferrite grain imaged in Figure 7 is the same grain from which the Figure 6 TEM was performed, but at lower magnification. The precipitates observed in Figure 6 are also seen in the δ ferrite grain in Figure 7; these precipitates are best seen in Figure 7d (the Ni map) as small dots within the elongated δ grain, indicating the precipitates contain Ni. Figure 7d demonstrates that these precipitates are uniformly distributed from the surface to a depth of approximately 10 μm within the irradiated δ ferrite. Moreover, no obvious evidence shown in Figure 7 that same type of precipitates is seen in irradiated γ austenite. It seems that these precipitates are favored to precipitate in proton irradiated δ ferrite rather than γ austenite.

3.3 Elemental segregation and precipitation in 308L filler material induced by proton irradiation

3.3.1 Elemental segregation and G-phase precipitation in δ Ferrite

Figure 8a is an HAADF image that includes two γ austenite grains and two δ ferrite grains of irradiated 308L filler material at a depth approximately 10 μm below the irradiated free surface. Voids are observed in the irradiated γ-austenite, indicated in Figure 8a. Figure 8b is a STEM-EDS

elemental line scan between the γ austenite grains along the cyan arrow in Figure 8a. Figures 8c-g are EDS elemental maps from the rectangular region indicated in Figure 8a. This region contains a γ–γ grain boundary and several twin boundaries. Cr depletion can be seen along the γ-γ grain boundary (Figure 8b) and along twin boundaries inclined approximately 45 degree to the γ-γ grain boundary in Figure 8d. Ni enrichment is observed at these same boundaries in Figure 8e. Cr depletion, Ni and Si enrichment is more prominent in the STEM-EDS line scan profile in Figure 8b. In summary, the γ-γ grain boundaries are depleted in Cr and Mn and enriched in Ni and Si. This observation is consistent with Jiao's findings [11, 16] and is due to the inverse Kirkendall effect. Ni, Si, and Mn enriched particles are detected in δ ferrite grains; these are evident from Figs. 8e, 8f and 8g. These precipitates are identified as G-phase precipitates based on STEM-EDS, HR-STEM and TEM-SAD presented below.

Figure 9a is a higher magnification HAADF image acquired in an irradiated δ ferrite grain showing cuboid 20 nm G-phase precipitates enriched in Ni, Si, and Mn, as Figs. 9d-f demonstrate. These precipitates are also poor in Fe and Cr (Figs. 9b and c). It is interesting that these precipitates, which are Ni rich, exist in the Ni-poor δ ferrite phase. Clearly enhanced diffusivity of Ni must exist during irradiation to facilitate precipitate growth. Lattice structure (black lines) of δ ferrite can be clearly seen in the HAADF image (Figure 9a). The δ ferrite lattice shows significant strain near the G-phase and it is clear that the two lattices are distinct.

High resolution STEM micrographs are shown in Figure 10. These images show the structural correlation between the G-phase and host δ ferrite lattice. Inset of Figure 8a indicates that $[001]_G//[001]_\delta$ correlation exists. Figure 10b is a small section from Figure 10a at higher magnification. STEM micrographs have mass contract, with heavier elements appearing brighter. This allows us to distinguish different elements in the high resolution micrographs and overlay the

G-phase and δ ferrite [001] lattice planes in Figures 10b and 10c. It is clear that both phases are commensurate with a lattice parameter ratio very close to 4:1.

Figure 11a is a bright field TEM micrograph imaged from the proton irradiated 308L filler at a depth of approximately 10 μm showing both δ ferrite and γ austenite grains. G-phase precipitates (tiny black dots) are observed in the δ ferrite grains. The parallel bands in γ austenite grains are twin boundaries. Two commensurate sets of diffraction patterns are observed in Figure 11b. The diffraction patterns of the δ ferrite (yellow dashed box) and G-phases $Mn_6Ni_{16}Si_7$ (cyan dashed box) showed a lattice ratio of 4:1 along the [113] zone axis of the micrograph. This agrees with our observation in Figure 10 and allows us to conclude the precipitates in proton irradiated δ ferrite is G phase ($Mn_6Ni_{16}Si_7$).

3.3.2 Irradiation Behavior in γ Austenite

Voids are observed in proton irradiated γ austenite, as shown in Figure 12a. STEM-EDS line scan was performed across a void, as indicated in the bottom left inset of Figure 12a. The line scan map in the top left inset of Figure 12a shows that all the elements in the void region (around 30 μm) are depleted, as expected. In addition, the Ni and Si signals peak at the edge of voids. The STEM-EDS map in Figure 12b-12f demonstrate that all elements are absent from the regions attributed to voids, again as expected. These maps also show Ni and Si enrichment around the periphery of the voids, indicating the void-matrix boundaries are energetically favorable to Ni and Si segregation. Jiao *et al*. observed Ni and Si enrichment around the irradiation induced Frank loops [11] and we suspect a similar phenomenon near voids in our irradiated 308L material.

Figure 13a is a STEM-HAADF micrograph of proton irradiated γ austenite at a depth of approximately 10 μm. The circled black spots in Figure 13a are voids in proton irradiated γ austenite. These voids (circled) appear as white spots in bright field TEM, as shown in Figure 13b.

A region including these white spots was captured by SAD, shown in the inset of Figure 13b. The diffraction patterns were taken along the [103] zone axis of γ austenite. Figure 13b demonstrates that only single set of sharp reflections from the FCC γ austenite are observed. This observation together with the lack of all elements in the mapped regions in Figure 12 allows us to confirm that these features are voids. We also note the Ni-Si enrichment at the edge of voids does not contribute in the SAD patterns, although the sensitivity to diffraction was low.

4. Discussion

4.1 Microstructural Morphology of As-Received and Irradiated 308L Weldment Filler

Two phases, δ ferrite and γ austenite, are present in the 308L weldment filler material. The percentage, morphology and distribution of δ ferrite precipitation upon cooling are directly related to both the composition of 308L filler and the cooling rate of the welding process [10, 32]. The ferrite content in stainless steels can be predicted using a Schaeffler diagram, such as that shown in Figure 14 [32, 33]. According to the composition of the 308L filler material studied here (see Table 1), the Ni equivalent and Cr equivalent of 308L filler is 11.84 and 20.64, respectively. The red dot in Figure 14 corresponds to our 308L composition, indicating 9% δ ferrite precipitation is expected. This is in good agreement with our EBSD data that quantified the δ ferrite phase fraction of 8.8%.

Cooling rate plays a critical role in the shape and morphology of δ ferrite in 308L filler. The microstructure of δ ferrite can have cellular structure, skeletal shape, and/or lathy morphology depending on the cooling rate [10]. A fast cooling rate yields a cellular structure of δ ferrite and a slow cooling rate leads to a skeletal morphology of δ ferrite [10]. The cooling rate in the process preparing SA508-304L DMW for this study was below 70 °C/h, which is slow enough to generate skeletal δ ferrite; this morphology is observed here (Figure 2a and Figure 3a).

4.2 Lattice Parameters of δ Ferrite and γ Austenite in 308L Weld Joint

Lattice parameter a of a crystal with cubic structure can be written as [34]:

$$a = d_{hkl}\sqrt{h^2 + k^2 + l^2} \tag{4.1}$$

Table 2 presents the lattice parameters of BCC Fe, FCC Fe, δ ferrite and γ austenite. According to Figure 3b, the measured $d_{1\text{-}10}$ of δ ferrite is 0.200 nm. Based on the equation 4.1, the calculated

$a_{ferrite}$ equals 0.283 nm, which agrees well with that of BCC Fe (0.286 nm) [35] and that of δ ferrite (0.286 to 0.290 nm) [28]. In addition, the measured $d_{11\text{-}1}$ in Figure 3c of γ austenite is 0.204 nm. According to equation 4.1, the calculated $a_{austenite}$ is 0.353 nm, which agrees to that of FCC Fe (0.356 nm) [36] and that of γ austenite (0.361 nm) [29]. Moreover, no additional diffraction reflections were seen in Figure 3 SAD patterns, indicating no additional precipitates in either unirradiated δ ferrite or γ austenite 308L filler material occurred. Voids were not observed in the unirradiated 308L filler either.

4.3 Effect of proton irradiation on mixed Phase in 308L filler

Proton irradiation induced different microstructural changes in the two 308L phases (δ ferrite and γ austenite). Specifically, G-phase precipitates were observed in δ ferrite, while voids and Ni-Si enriched clusters were observed in γ austenite. The possible reasons for the different microstructural features induced by proton irradiation are discussed in the following sections.

4.3.1 G-phase precipitates in proton irradiated δ ferrite

G phase precipitates were observed in irradiated δ ferrite, as shown in the SEM micrograph of Figure 5b. On the other hand, precipitation was not observed in the irradiated γ austenite as seen in Figure 5b, or unirradiated δ ferrite as shown in Figure 3b. This is confirmed by STEM-EDS maps in Figure 8, where Mn-Si-Ni rich precipitates (confirmed to be G phase particles via TEM-SAD in Figure 11) are observed in δ ferrite, but no evidence of precipitates in γ austenite is found. In addition, these Ni-Si-Mn precipitates were uniformly distributed in the irradiated δ ferrite, as demonstrated in Figure 7d (STEM-EDS Ni map). The length of the skeletal δ ferrite grain seen in Figure 7d is approximately 10 μm and the top of the δ ferrite grain is close to the free surface of TEM specimen. TRIM simulations of 2 MeV protons on 308L (Figure 4) demonstrate that the energy to recoils increases by about a factor of two from the free surface to a depth of 15 μm. The

corresponding displacements per atom (dpa) increases from approximately 3 to 5 dpa. The effect of dpa damage with respect to G phase precipitation in δ ferrite and elemental segregation/depletion saturates from the free surface to a depth of 10 μm. This coincidentally is about the same size of the TEM lift out specimen. This statement is based on the observed uniformity of precipitation versus depth. Further, our STEM-EDS elemental maps, in particular the uniform map of Ni in δ ferrite (Figure 7d) is consistent with a microstructure which has reached saturation with respect to dpa damage.

The lattice parameter of δ ferrite in 308L filler specimen is 0.290 nm STEM HR micrograph in Figure 10c. This lattice parameter is comparable to the more accurate determination from the Figure 3b SAD pattern (0.283 nm). Slight distortions during high resolution STEM image acquisition is likely responsible for the discrepancies of lattice parameters. The diffraction patterns from Figs. 6a and 11b confirmed the lattice parameter ratio between the G and δ ferrite phases as 4 to 1. A simulated G phase ($Mn_6Ni_{16}Si_7$) crystal structure is shown in Figure 10b along the [100] zone axis agrees well with the HR-STEM micrograph of Ni-Si-Mn precipitates (Figure 10b). The lattice parameter of G phase precipitates calculated from Figure 11b is 1.072 nm, which is approximately 4 times larger than that of δ ferrite (0.290 nm). It is also comparable to that measured by others (1.109 nm) [37].

Analysis of STEM-EDS spectra from the G phase precipitates embedded in the δ ferrite matrix (Figure 9) indicates an average composition for both phases of 30.6 at.% Ni, 10.4 at.% Si, 10.5 at.% Mn, 13.8 at.% Cr, and 34.7 at.% Fe. We assume the Cr signal (13.8 at.%) is from the matrix of δ ferrite only. Based on this assumption, we can attribute 31.8 at.% Fe, 13.8 at.% Cr, 1.8 at.% Ni, 0.2 at.% Si, and 0.45 at.% Mn of the EDS spectra analysis to the δ ferrite matrix from the know composition of δ ferrite. This then suggests that nearly all the detected Fe signal is from the δ

ferrite matrix (31.8 at.% vs. 34.7 at.%). Therefore, we calculate the composition of the precipitates as 20.4 at.% Mn, 58.8 at.% Ni, and 20.8 at.% Si, with some Fe substituting for Ni. This is in reasonable agreement with the known G phase stoichiometry $Mn_6Ni_{16}Si_7$ (6:17:7).

The G phase precipitates have strong contrast in the dark field TEM (Figure 6). The TEM dark field TEM micrograph in Figure 6 was imaged from the weaker set of reflections rather than the strong δ ferrite matrix reflections. The diffraction patterns were taken along the [100] zone axis. In order to index the G phase particles in irradiated δ ferrite accurately, the δ ferrite matrix was tilted to a different zone axis to reveal diffraction spots from the G phase precipitates. When the δ ferrite grain was tilted to the [113] zone axis, the number of G phase reflections reached a maximum, as seen in Figure 11b. The reflections from FCC G phase and BCC δ ferrite appear commensurate along this zone axis. The d-spacing of the G phase (220) plane is 0.172 nm, while that of the δ ferrite (110) plane is two times smaller (0.086 nm).

The question remains as to why the system chooses the δ-ferrite phase over the γ-austenite phase for G phase precipitation. The G phase lattice parameter (1.109 nm) is nearly commensurate with δ ferrite (0.283 nm) and this may lead to a reduced interfacial energy and act to reduce the volumetric strain energy associated with an embedded precipitate. Thus G phase precipitation in δ ferrite is favored based interfacial energy considerations when the system has a choice of host matrices. In the following section, DFT calculations are used to quantitatively compare the interface energies for G phase in different Fe phases.

4.3.2 Theoretical explanation of G phase formation in BCC and FCC Fe

In our experiments, it is found that $Mn_6Ni_{16}Si_7$ G phase only forms in δ ferrite but not in γ austenite in the duplex 308L stainless steel under proton irradiation. Previously, Chen et al. [38] reported that in thermally-aged CF8 cast austenitic stainless steels in which both δ ferrite and γ

austenite exist, the G-phase precipitates were only observed in δ ferrite. Upon heavy-ion irradiation, new G-phase precipitates were observed in δ ferrite matrix but not in γ austenite. Recently, Lin et al. [21] also reported that Mn-Ni-Si rich G phase formed in δ ferrite but not in γ austenite in proton-irradiated 308L. In addition, G phase formation was also observed in thermally treated ferritic steels [39]. These experimental studies suggest that G phase may be energetically more favorable to form in Fe based alloys with a BCC structure (that is, α and δ ferrite) than those with a FCC structure (γ austenite), although this hypothesis has never been proven to our best of knowledge. Here density functional theory (DFT) modeling is used to calculate the interface energies of both G/FeBCC and G/FeFCC interfaces, providing a theoretical explanation of the experimental observations.

As described in the Method Section, we considered different magnetic states for G/Fe interfaces. Three scenarios are considered: 1) both Fe and G phase are non-magnetic (NM), 2) both Fe and G phase are ferromagnetic (FM), and 3) Fe is a paramagnetic (PM) and G phase is ferromagnetic (FM). In each of these three scenarios, both BCC and FCC Fe are modeled. Therefore, a total of six different types of interface systems with different magnetic states and Fe phases are modeled.

To use Equation (2.1) to calculate the interface energies, the energies of bulk BCC Fe, FCC Fe, and $Mn_6Ni_{16}Si_7$ G phase of the same magnetic states as in the interface systems are needed. For G phase, both NM and FM states are modeled. The relaxed structures are shown in Figure 15. The structures based on the two magnetic states are similar, although slight discrepancy can be seen regarding the Mn and Si arrangements between two neighboring polyhedrals, as indicated by the red arrow in each figure. It should be noted that the structure based on the FM state (Figure 15b) agrees very well with the refined structure from neutron diffraction experiments [24]. The

predicted lattice parameter is 10.98 Å for the NM state and 11.10 Å for the FM state in this work. The latter is in very good agreement with the experimental value of 11.12 Å at 4 K [24] and previous DFT result of 11.10 Å [24]. In addition, the energy of the G phase in the FM state is about 2.89 eV per $Mn_6Ni_{16}Si_7$ formula unit lower than that in the NM state. Therefore, the G phase in the FM state is more consistent with the experimental results than the NM state.

Three magnetic states are modeled for each of BCC and FCC Fe: NM, FM, and PM. The lattice parameter (a_0) and the relative energy with respect to the ground state Fe for each configuration is shown in Table 4. For BCC Fe in the FM state (BCC-FM), which is the ground state and represents α-Fe, the predicted lattice parameter a_0 = 2.83Å is in good agreement with the experimental value of 2.86Å [35]. For non-magnetic BCC Fe (BCC-NM), the predicted lattice parameter a_0 = 2.76Å is smaller than that of α-Fe and the energy is significantly higher (0.472 eV/atom) than α-Fe. For BCC Fe in the PM state (BCC-PM), which is considered to be the δ-Fe surrogate in this work, the predicted lattice parameter a_0 = 2.83Å is identical as our experimental value of 2.83Å. The energy is slightly higher (0.169 eV/atom) than α-Fe. FCC Fe in the PM state (FCC-PM) represents the γ-Fe in this work and the predicted lattice parameter is a_0 = 3.49Å, which is close to our experimental value of 3.53Å. The energy for this structure is slightly higher than α-Fe by 0.133 eV/atom, but is lower than that of δ-Fe. For FCC in NM (FCC-NM) and FM (FCC-FM) states, the predicted a_0 is either lower or higher than the experimental value of γ-Fe, and the respective energies are also slightly higher than the γ-Fe in the PM state. The lattice parameters simulated with DFT are listed in Table 2. Overall, our DFT modeling predicts that the phase order is α (FM) < γ (PM) < δ (PM) based on eV/atom energies, which is consistent with the experimentally observed stability sequence (α→γ→δ) as the system temperature is increased. These phases are highlighted in bold in Table 4.

The G/Fe interface energies for different combinations of magnetic states and Fe crystal structure are calculated using Equation (2.1) and the results are listed in Table 5. Two representative interface structures, G/Fe_{BCC} and G/Fe_{FCC}, are shown in Figure 16 for illustration. For Case 1 in which both Fe and G phase are non-magnetic (note the reference systems are also non-magnetic for interface energy calculation), the interface energy of G/Fe_{BCC} is -1.06 J/m^2, while that of G/Fe_{FCC} is 1.14 J/m^2. The negative G/Fe_{BCC} interface energy seems surprising because an interface made of the same material (e.g., grain boundaries) always has a positive energy. However, for a heterogeneous interface made of dissimilar materials such as θ–Al_2O_3 + water, a negative interface energy has been reported experimentally [40] because of the chemical reaction and formation of new bonds between dissimilar materials [41]. The negative interface energy means that the formation of such a heterogeneous interface is an exothermic process and the resulting interface bonds are very strong [41]. Therefore, the negative interface energy of the non-magnetic G/Fe_{BCC} is likely due to the strong chemical effect at this heterogeneous interface. It also suggests that the precipitation of G interface in a BCC Fe matrix, if both are non-magnetic, is a spontaneous process. On the other hand, nucleation of the G phase in a FCC Fe matrix, if both are non-magnetic, has to overcome the large positive interface energy.

For Case 2 in which both Fe and G phase are ferromagnetic (note the reference systems are also ferromagnetic), the interface energy of G/Fe_{BCC} is 0.68 J/m^2, while that of G/Fe_{FCC} is 0.84 J/m^2. Again, the interface energy between BCC Fe and the G phase is lower compared to FCC Fe and the G phase, although the difference is small. Note here the ferromagnetic G/Fe_{BCC} interface can be related to the precipitation of G phase in a ferritic α-Fe matrix. This interface energy is moderate so that the formation of G phase in a ferritic α-Fe is possible. This prediction is

consistent with some experimental observations of G phase formation in ferritic Fe-based steels upon heat treatment [39].

To model the more complex Case 3 in which Fe is a paramagnetic and G phase is ferromagnetic, the initial interface system consists of a non-magnetic BCC or FCC Fe and a ferromagnetic G phase. Since the spin polarized DFT is used, BCC or FCC Fe atoms gain some magnetic moments automatically after relaxation. The magnetic moments of these Fe atoms are either positive or negative and the magnitudes vary significantly. Therefore, the magnetic states of BCC and FCC Fe in the interface system upon relaxation can be approximated as the paramagnetic state, as we do for bulk BCC δ-Fe (PM) and FCC γ-Fe (PM). To calculate the interface energies, both non-magnetic and paramagnetic Fe are considered as the reference systems to check how the interface energy is sensitive to the magnetic state of Fe. When the non-magnetic BCC Fe is used as a reference system, which is the initial condition of Fe before the interface is relaxed, the calculated G/Fe_{BCC} interface energy is -2.22 J/m^2, a very low value due to the high energy of BCC-NM Fe (Table 4). This value can be considered as a lower limit of the interface energy for G/Fe_{BCC} since the magnetic states of Fe in the relaxed interface system are not exactly the same as in the reference bulk Fe. When the paramagnetic BCC Fe is used as a reference system, which is close to the final state of Fe after the interface is relaxed, the calculated G/Fe_{BCC} interface energy is 0.35 J/m^2. As the Fe is in a nearly paramagnetic state in this relaxed interface system, this interface energy is the most relevant case to the G phase precipitation in δ-Fe observed in our experiments. Since FCC-PM γ-Fe is more stable than BCC-PM δ-Fe and the former has a lower energy than the latter (Table 4), we also can use the energy (per atom) of FCC-PM γ-Fe as the reference energy to determine the upper limit of the G/δ-Fe interface energy. The calculated value is 0.66 J/m^2, as shown in Table 5. For the interface energy between FCC Fe and paramagnetic G phase (G/Fe_{FCC}), the

calculated value is 1.05 J/m^2 if the non-magnetic FCC Fe is used as the reference system, and 1.25 J/m^2 if the paramagnetic FCC Fe is used as the reference system. The difference is not as significant as for the G/Fe$_{BCC}$ interface. The latter value (1.25 J/m^2) can be considered to be the interface energy for a G phase precipitation in the γ-Fe. Comparing the interface energy between G/Fe$_{BCC}$ and G/Fe$_{FCC}$ in Case 3, the G/Fe$_{BCC}$ always has a much lower interface energy, even at the upper limit.

Table 5 lists the interface energies for different combinations of G phase and Fe. Regardless of which magnetic state is assumed, the G/Fe$_{BCC}$ interface energy is always lower than that of G/Fe$_{FCC}$. Considering the known magnetic states in α, γ, and δ Fe, the interface energy should be 0.68 J/m^2 for α/G, 1.25 J/m^2 for γ/G, and 0.35 J/m^2 for δ/G. These interface energies are highlighted in bold in Table 5. Therefore the interface energy in δ-Fe is smallest and that in γ-Fe is largest. If δ-Fe and γ-Fe phases coexist in steels, such as in 308L studied in this work, the G phase will preferentially precipitate in δ-Fe rather than in γ-Fe based on interface energy considerations. Therefore, our DFT calculations provide a thermodynamics-based explanation for the preferential precipitation of the G phase in δ ferrite but not in γ austenite. This conclusion holds for both in our experiments as well as other observations in the published literature [38].

For comparison we can calculate the bulk strain energy associated with misfit interfacial lattice strain u_{coh} given by,

$$u_{coh} = 2\mu\left(\frac{1+\upsilon}{1-\upsilon}\right)h\varepsilon^2, \tag{4.2}$$

where μ is the shear modulus, υ is Poisson's ratio, h is the thickness, and ε is the misfit strain. The multiplication by h leads to units of energy per area [42]. The shear modulus (91, 81, and 80 GPa)

and Poisson's ratio (0.28, 0.33, and 0.31) values were used for the G-phase, γ-austenite, and δ-ferrite, respectively [bjh1]. Equation 4.2 is derived assuming two cubic lattices oriented along the [100] direction, as is the case here. The misfit strains between the G-phase lattice and either FCC-γ or BCC-δ lattice are 0.012 and -0.053, respectively, using our measured lattice parameters of the two phases (Table 2). The misfit strain dominates the comparison since the elastic properties of the three systems do not differ significantly. We use the G-phase supercell thickness, corresponding to one unit cell, for *h*. The bulk strain energies are 0.05 and 0.92 J/m^2 for the G-phase//γ and G-phase// δ, respectively. An alternative estimation of the bulk strain energy can be obtained by a simple integration of Hooke's Law assuming completely elastic behavior. This leads to an equation similar to Eq. 4.2, but reduced by a factor of 2/(1-ν). The corresponding to bulk strain energies are 0.02 and 0.07 J/m^2 for the G-phase// γ and G-phase// δ, respectively. It is not surprising that misfit strain energy would favor precipitation in the austenitic phase given the lower lattice misfit. However, the electronic/magnetic factors captured by the DFT computations must govern the observed precipitation. We note also that the DFT computations implicitly include lattice misfit strain effects since the interfacial coherency was maintained in the supercell.

We also note that the self-diffusivity in BCC is significantly larger (around 100 times larger) than in FCC [43-46]. Therefore the kinetics may also play a role on the G phase formation in δ ferrite, although the radiation-enhanced diffusion could provide sufficient diffusion kinetics of G-phase elements in both δ ferrite and γ austenite. As mentioned earlier, actually G phase formation was observed in ferritic α-Fe matrix [39], even though α-Fe has a lower self-diffusivity than δ-Fe [47] and possibly γ-Fe as well. The interface energy in α-Fe is moderate (0.68 J/m^2) according to our DFT calculations so precipitation of G phase in α-Fe is thermodynamically possible.

Therefore, we believe the interface energy plays a major role in determining if G phase can precipitate in different Fe phases.

4.3.3 Voids and elemental segregation to voids, δ/γ and γ/γ boundaries

Irradiation induced voids were only observed in γ austenite, as seen in Figure 8a, Figure 12 and Figure 13. In the irradiated dual phase region of 316 stainless steel, it has been reported that the void swelling rate in FCC γ austenite is much higher than that of irradiated BCC phase at 673 K [48]. Therefore, ferritic steels with BCC lattice structure are less susceptible to swelling than austenite steels with FCC crystal structure under irradiation [49]. Moreover, the diffusivity of solutes in γ austenite is 4 orders [50-52] of magnitude lower than that in δ ferrite at the same temperature. Furthermore, the thermal expansion coefficient of FCC austenitic steels is higher than that of BCC ferritic steels [53, 54]. Consequently, the difference in thermal expansion leads to stress near δ/γ boundaries. It has been reported that both compressive stress and tensile stress contributed to accelerate the void swelling rate of irradiated FCC 316L stainless steels [55, 56]. Therefore, the stress introduced by thermal expansion difference in the γ austenite could make γ austenite even more vulnerable to void swelling under proton irradiation.

We observe the segregation of Si and Ni to voids in Figure 12. It has been shown that Si has a large binding energy with other solutes in Fe-based alloy systems [12], yielding a decrease of diffusivity of other solutes as the composition of Si increases [57]. The binding of Si to other solutes can result in the segregation of Si to sinks such as grain boundaries and void surface as these other solutes diffuse to the same sinks [12, 58]. In addition, the bulk (lattice) diffusivity of solutes can be 5 orders of magnitude lower compared to the diffusivity at defects such as dislocations, grain boundaries, and other interfacial defects [59-61]. Both effects will promote the co-segregation of Ni and Si to void surfaces and grain boundaries.

The SAD pattern from the proton irradiated γ austenite containing voids is shown in Figure 13b. This pattern contains only γ austenite reflections, implying the Ni and Si segregation to voids does not lead to the precipitation of a second phase. It is also possible that the density of these Ni-Si enriched regions is too low to produce diffraction patterns. The Ni-Si enriched regions are unlike to represent the precipitation of the G phase in proton irradiated δ ferrite. We notice that the Ni-Si segregation regions are not enriched with Mn. Ni-Si enriched clusters are reported in irradiated γ austenite by other researchers as well [11, 16]. We believe this segregation represents the precursors to γ', which may have formed with longer irradiation time and greater dpa.

In addition, segregation of Ni, Si and Mn at γ/γ and δ/γ boundaries is observed, as shown in Figs. 8e, 8f and 8g. The γ/γ boundary is enriched with Ni and Si but depleted in Mn, which is similar to the Ni-Si segregation to void surfaces in γ austenite. This observation suggest the segregation/precipitation behavior near the γ/γ boundary and at void surfaces in irradiated γ austenite is similar. In contrast, Mn enrichment is detected only at δ/γ boundaries, as shown in Figure 8g. We believe that the segregation observed at the δ/γ boundaries can be explained by the fact that grain boundaries are solute sinks and the fact that Mn segregation in irradiated δ ferrite is favored based on the observed G-phase precipitation.

5. Conclusions

The effect of proton irradiation to a level of 3 to 5 dpa on the microstructure of 308L weldment groove filler material has been studied. The filler material in a weldment recrystallizes into a mixed or dual phase microstructure containing both skeletal δ ferrite and γ austenite. We observe the expected segregation of Ni and Si to grain and twin boundaries in γ austenite and as well as the expected Cr depletion. In addition, G phase formation ($Mn_6Ni_{16}Si_7$) is observed in δ ferrite but not in γ austenite. This is somewhat surprising since δ ferrite is largely devoid of these elements. However, proton irradiation induces significant solute transport and DFT computations we perform demonstrate that the G phase interfacial energy is lowest in the δ phase matrix. Proton irradiation also induced void formation in the γ austenite, consistent with the known irradiation induce swelling of FCC stainless steels. Segregation of Ni and Si to the void-matrix interfaces was observed. The groove filler material is suspected as the source of IASCC of LWR weldment repairs and the precipitate hardening associated with G phase formation may be an influencing factor. Specific details of our work follow:

1. G phase $Mn_6Ni_{16}Si_7$ precipitation with FCC structure is confirmed with HR-STEM microscopy, by TEM dark field selected area diffraction patterns, and STEM-EDS spectra analysis. $Mn_6Ni_{16}Si_7$ precipitates are detected only in δ ferrite after proton irradiation, which can be attributed to (1) a much higher diffusivity (2 orders of magnitude higher at the same temperature) of Ni in BCC structure than that in FCC structure and (2) the energetically favorable nature due to lattice match with host matrix, δ ferrite.

2. DFT calculations are performed to calculate the interface energy between $Mn_6Ni_{16}Si_7$ G-phase and Fe. Six different magnetic state-crystal lattice structures were considered for the G phase-Fe interface. The G/Fe_{BCC} interface always exhibited a lower interface energy compared to the G/Fe_{FCC} interface. For the three Fe phases in the equilibrium phase diagram, our DFT results show that the G/Fe interface energy is in the following order: δ/G (0.35 J/m^2) < α/G (0.68 J/m^2) < γ/G (1.25 J/m^2). Therefore, it is energetically favorable to form the G-phase in the δ-Fe matrix rather than in γ-Fe when the two phases coexist, such as in the 308L studied in this work. Although kinetics and the chemical potential or Gibbs free energy driving force could also play a role, our DFT results provide a very reasonable thermodynamics based explanation of the preferential formation of G phase in δ ferrite under irradiation or thermal annealing.
3. Ni-Si enriched regions were detected at the interfaces of irradiation induced voids in γ austenite. Higher diffusivity of Ni at defect sinks, such as voids and grain boundaries may promote Ni-Si bonding at sink such as voids and other interfacial boundaries. Further, the voids are point defect sinks and the inverse Kirkendall effect will lead to the observed segregation. These the Ni-Si enriched regions are poor in Mn and we believe they are precursors to the γ' phase known to precipitation in austenitic stainless steels during irradiation.
4. In addition, the depletion of Cr and the enrichment of Ni and Si is observed at γ/γ grain boundaries and twin boundaries in γ austenite, while Ni, Si and Mn enrichment is observed at δ/γ boundaries. The segregation of Ni and Si and the depletion of Cr at grain boundaries is consistent with the well-known behavior of these elements in austenitic stainless steel due to the inverse Kirkendall effect, referred to as radiation-induced segregation (RIS).

The depletion of Cr via RIS is thought to be an influential factor in IASCC. Early LWR operational experience connected RIS-induced Cr depletion to IASCC in austenitic stainless steel [62]. However, Cr depletion is not the only contributing factor and localized deformation has been implicated as well [63]. Further, boron segregation and small defect (black dot) clusters may also play a role [63]. IASCC is currently thought to be controlled by a combination of factors, including environmental exposure (water chemistry and radiolysis), localized deformation, tensile stress, RIS, and radiation damage.

6. Acknowledgement

This work was supported by the US Department of Energy Nuclear Energy University Programs (NEUP) under contract number DE NE0008699. A portion of the experiments presented here were carried out at the Materials Research Laboratory Central Research Facilities, University of Illinois. The Michigan Ion Beam Laboratory was used to perform the proton irradiation exposures. The authors are grateful to Drs. Gary Was and Ovidiu Toader for support in performing the irradiations, as well as Dr. Miao Song for help with sample electropolishing prior to proton irradiation. X.M.B. at Virginia Tech acknowledges the subcontract of this NEUP project from the University of Illinois, and the Faculty Joint Appointment Program at Idaho National Laboratory. The DFT modeling by X.M.B. made use of the resources of the High Performance Computing Center at Idaho National Laboratory, which is supported by the Office of Nuclear Energy of the U.S. Department of Energy and the Nuclear Science User Facilities under Contract No. DE-AC07-05ID14517.

7. Contribution

Zhen Li: Experiments, Methodology, Investigation, Writing-Original draft preparation. Xun Zhan: HR-STEM, Formal data analysis, Reviewing and Editing. Xian-Ming Bai: DFT Simulation, Writing, Reviewing and Editing. Shao-Chun Lee: DFT Simulation, Reviewing. Weicheng Zhong: EBSD, Reviewing and Editing. Benjamin J. Sutton: Weldment preparation, Reviewing. Brent J. Heuser: Funding acquisition, Supervision, Conceptualization, Writing, Reviewing, and Editing.

References

1. Seifert, H.P., et al., *Environmentally-assisted cracking behaviour in the transition region of an Alloy182/SA 508 Cl.2 dissimilar metal weld joint in simulated boiling water reactor normal water chemistry environment.* Journal of Nuclear Materials, 2008. **378**(2): p. 197-210.
2. Kim, S., et al., *Effects of alloying elements on mechanical and fracture properties of base metals and simulated heat-affected zones of SA 508 steels.* Metallurgical and Materials Transactions A, 2001. **32**(4): p. 903-911.
3. Ming, H., et al., *Microstructural characterization of an SA508–309L/308L–316L domestic dissimilar metal welded safe-end joint.* Materials characterization, 2014. **97**: p. 101-115.
4. Niu, W., et al., *Stress–Corrosion Cracking of Surface-Engineered Alloys in a Simulated Boiling-Water Reactor Environment.* Corrosion, 2018. **74**(6): p. 635-653.
5. McMinn, A., *Stress corrosion of high-chromium nickel-base weld metals and AISI 316 nuclear grade stainless steel in simulated boiling water reactor environments.* Corrosion, 1986. **42**(11): p. 682-689.
6. Garcia, C., et al., *Stress corrosion cracking behavior of cold-worked and sensitized type 304 stainless steel using the slow strain rate test.* Corrosion, 2002. **58**(10): p. 849-857.
7. Andresen, P.L. and G.S. Was, *A historical perspective on understanding IASCC.* Journal of Nuclear Materials, 2019.
8. Song, M., et al., *Radiation damage and irradiation-assisted stress corrosion cracking of additively manufactured 316L stainless steels.* Journal of Nuclear Materials, 2019. **513**: p. 33-44.
9. Li, G. and J. Congleton, *Stress corrosion cracking of a low alloy steel to stainless steel transition weld in PWR primary waters at 292 C.* Corrosion Science, 2000. **42**(6): p. 1005-1021.
10. Brooks, J. and A. Thompson, *Microstructural development and solidification cracking susceptibility of austenitic stainless steel welds.* International Materials Reviews, 1991. **36**(1): p. 16-44.
11. Jiao, Z. and G. Was, *Novel features of radiation-induced segregation and radiation-induced precipitation in austenitic stainless steels.* Acta Materialia, 2011. **59**(3): p. 1220-1238.
12. Brager, H. and F. Garner, *Swelling as a consequence of gamma prime (γ') and M23 (C, Si) 6 formation in neutron irradiated 316 stainless steel.* Journal of Nuclear Materials, 1978. **73**(1): p. 9-19.
13. Maziasz, P., *Formation and stability of radiation-induced phases in neutron-irradiated austenitic and ferritic steels.* Journal of Nuclear Materials, 1989. **169**: p. 95-115.
14. Kanematsu, K., *Stability of Crystal Structure of (Fe, V) 3M and (Fe, Ni) 3M (M= Si, Ge, Sn) and Its Analysis Based on Rigid Band Model.* Transactions of the Japan institute of metals, 1986. **27**(4): p. 225-232.
15. Toyama, T., et al., *Irradiation-induced precipitates in a neutron irradiated 304 stainless steel studied by three-dimensional atom probe.* Journal of nuclear materials, 2011. **418**(1-3): p. 62-68.
16. Jiao, Z., J. Hesterberg, and G. Was, *Effect of post-irradiation annealing on the irradiated microstructure of neutron-irradiated 304L stainless steel.* Journal of Nuclear Materials, 2018. **500**: p. 220-234.

17. Li, Z., et al., *Irradiation response of delta ferrite in as-cast and thermally aged cast stainless steel.* Journal of Nuclear Materials, 2015. **466**: p. 201-207.
18. Ward, A., *Irradiation effects on mechanical properties of an SMAW deposited Type 308 stainless steel.* Weld J., 1975. **54**(8): p. 259.
19. Corwin, W., et al., *Fracture behavior of a neutron-irradiated stainless steel submerged arc weld cladding overlay.* Nuclear Engineering and Design, 1985. **89**(1): p. 199-221.
20. Lin, X., et al., *Irradiation-induced segregation at phase boundaries in austenitic stainless steel weld metal.* Scripta Materialia, 2018. **149**: p. 11-15.
21. Lin, X., et al., *Corrosion of phase and phase boundary in proton-irradiated 308L stainless steel weld metal in simulated PWR primary water.* Corrosion Science, 2020. **165**: p. 108401.
22. Mansur, L., *Theory and experimental background on dimensional changes in irradiated alloys.* Journal of Nuclear Materials, 1994. **216**: p. 97-123.
23. Ziegler, J.F., *The stopping and range of ions in matter*, in http://srim.org/. 2013.
24. Ahmed, S.J., et al., *Magnetic and Structural Studies of G-Phase Compound Mn6Ni16Si7.* Inorganic chemistry, 2018. **57**(22): p. 14144-14151.
25. King, D., et al., *G-phase strengthened iron alloys by design.* Acta Materialia, 2020. **183**: p. 350-361.
26. Kresse, G. and D. Joubert, *From ultrasoft pseudopotentials to the projector augmented-wave method.* Physical review b, 1999. **59**(3): p. 1758.
27. Perdew, J.P., K. Burke, and M. Ernzerhof, *Generalized gradient approximation made simple.* Physical review letters, 1996. **77**(18): p. 3865.
28. Niu, H. and I. Chang, *Microstructural evolution during laser cladding of M2 high-speed steel.* Metallurgical and Materials Transactions A, 2000. **31**(10): p. 2615-2625.
29. Li, Z., *Surface hardening of austenitic Fe-Cr-Ni alloys for accident-tolerant nuclear fuel cladding*. 2018, Case Western Reserve University. p. 155.
30. Li, Z., et al., *Surface engineering of IN-718 by low-temperature carburisation: properties and thermal stability.* Surface Engineering, 2019. **35**(3): p. 281-293.
31. Li, Z., et al., *Low-Temperature Carburization of AL-6XN Enabled by Provisional Passivation.* Metals, 2018. **8**(12): p. 997.
32. Schaeffler, A.L., *Constitution diagram for stainless steel weld metal.* Metal Progress, 1949. **56**(11): p. 680-680B.
33. Kou, S., *Welding Metallurgy Second Edition*. 2003, Hoboken, New Jersey: John Wiley & Sons, Inc.
34. Callister, W.D. and D.G. Rethwisch, *Materials science and engineering: an introduction*. 2011: John Wiley & Sons, Inc.
35. Yelsukov, E., E. Voronina, and V. Barinov, *Mössbauer study of magnetic properties formation in disordered Fe-Al alloys.* Journal of magnetism and magnetic materials, 1992. **115**(2-3): p. 271-280.
36. Schlosser, W., *Calculation of the atomic volumes of Fe-Ni and Fe-Co alloys.* physica status solidi (a), 1973. **17**(1): p. 199-205.
37. Kolenda, M., et al., *Magnetic properties of Mn6Ni16Si7 and Mn3Cr3Ni16Si7.* Journal of magnetism and magnetic materials, 1991. **96**(1-3): p. 121-124.
38. Chen, W.-Y., et al., *In situ TEM study of G-phase precipitates under heavy ion irradiation in CF8 cast austenitic stainless steel.* Journal of Nuclear Materials, 2015. **464**: p. 185-192.
39. Sun, W., et al., *G phase precipitation and strengthening in ultra-high strength ferritic steels: Towards lean 'maraging' metallurgy.* Acta Materialia, 2017. **130**: p. 28-46.

40. Łodziana, Z., N.-Y. Topsøe, and J.K. Nørskov, *A negative surface energy for alumina.* Nature materials, 2004. **3**(5): p. 289-293.
41. Łodziana, Z., N.-Y. Topsøe, and J.K. Nørskov, *Negative surface energy—clearing up confusion.* Nature Materials, 2005. **4**(3): p. 186-186.
42. Tsao, J., *Materials Fundamentals of Molecular Beam Epitaxy* 1993, San Diego, CA: Academic Press, Inc.
43. Fredriksson, H. and J. Stjerndahl, *Solidification of iron-base alloys.* Metal science, 1982. **16**(12): p. 575-586.
44. Hämäläinen, E., et al., *Mechanical properties of powder metallurgy duplex stainless steels.* Materials science and technology, 1997. **13**(2): p. 103-109.
45. Campos, M., et al., *Study of the interfaces between austenite and ferrite grains in P/M duplex stainless steels.* Journal of the European Ceramic Society, 2003. **23**(15): p. 2813-2819.
46. Mehrer, H., *Diffusion in solids: fundamentals, methods, materials, diffusion-controlled processes*. Vol. 155. 2007: Springer Science & Business Media.
47. James, D. and G. Leak, *Self-diffusion and diffusion of cobalt in alpha and delta-iron.* The Philosophical Magazine: A Journal of Theoretical Experimental and Applied Physics, 1966. **14**(130): p. 701-713.
48. Blasl, D., et al., *Void swelling and microstructure evolution of a dual phase (ferritic and austenitic) stainless steel.* Journal of nuclear materials, 1985. **133**: p. 517-520.
49. Garner, F., M. Toloczko, and B. Sencer, *Comparison of swelling and irradiation creep behavior of fcc-austenitic and bcc-ferritic/martensitic alloys at high neutron exposure.* Journal of Nuclear Materials, 2000. **276**(1-3): p. 123-142.
50. Jönsson, B., *Assessment of the mobilities of Cr, Fe and Ni in bcc Cr-Fe-Ni alloys.* ISIJ international, 1995. **35**(11): p. 1415-1421.
51. Cui, Y.-W., et al., *Computational study of atomic mobility for fcc phase of Co-Fe and Co-Ni binaries.* Journal of Phase Equilibria and Diffusion, 2008. **29**(1): p. 2-10.
52. Kucza, W., et al., *Studies of "sluggish diffusion" effect in Co-Cr-Fe-Mn-Ni, Co-Cr-Fe-Ni and Co-Fe-Mn-Ni high entropy alloys; determination of tracer diffusivities by combinatorial approach.* Journal of Alloys and Compounds, 2018. **731**: p. 920-928.
53. Leibowitz, L. and R. Blomquist, *Thermal conductivity and thermal expansion of stainless steels D9 and HT9.* International journal of thermophysics, 1988. **9**(5): p. 873-883.
54. Bogaard, R., et al., *Thermophysical properties of stainless steels.* Thermochimica Acta, 1993. **218**: p. 373-393.
55. Lauritzen, T., et al. *Irradiation-induced swelling in AISI 316 steel: Effect of tensile and compressive stresses*. in *Radiation-Induced Changes in Microstructure: 13th International Symposium (Part I)*. 1987. ASTM International.
56. Sahu, H. and P. Jung, *Void swelling and irradiation creep in stainless steel under compressive and tensile stress.* Journal of Nuclear Materials, 1985. **136**(2-3): p. 154-158.
57. Simonovic, D., et al., *Diffusion of carbon in bcc Fe in the presence of Si.* Physical Review B, 2010. **81**(5): p. 054116.
58. Little, E., *Void-swelling in irons and ferritic steels: I. Mechanisms of swelling suppression.* Journal of Nuclear Materials, 1979. **87**(1): p. 11-24.
59. Wazzan, A.R., *Lattice and grain boundary self‐diffusion in nickel.* Journal of Applied Physics, 1965. **36**(11): p. 3596-3599.

60. Paul, A. and R. Agarwala, *Lattice and grain boundary diffusion of cerium and neodymium in nickel.* Metallurgical Transactions, 1971. **2**(9): p. 2691-2695.
61. Suzuoka, T., *Lattice Diffusion and Grain Boundary Diffusion of Cobalt in γ-Iron.* Transactions of the Japan Institute of Metals, 1961. **2**(3): p. 176-181.
62. Andresen, P., et al., *State of knowledge of radiation effects on environmental cracking in light water reactor core materials*. 1991.
63. Busby, J., G. Was, and E. Kenik, *Isolating the effect of radiation-induced segregation in irradiation-assisted stress corrosion cracking of austenitic stainless steels.* Journal of Nuclear Materials, 2002. **302**(1): p. 20-40.

8. Figures

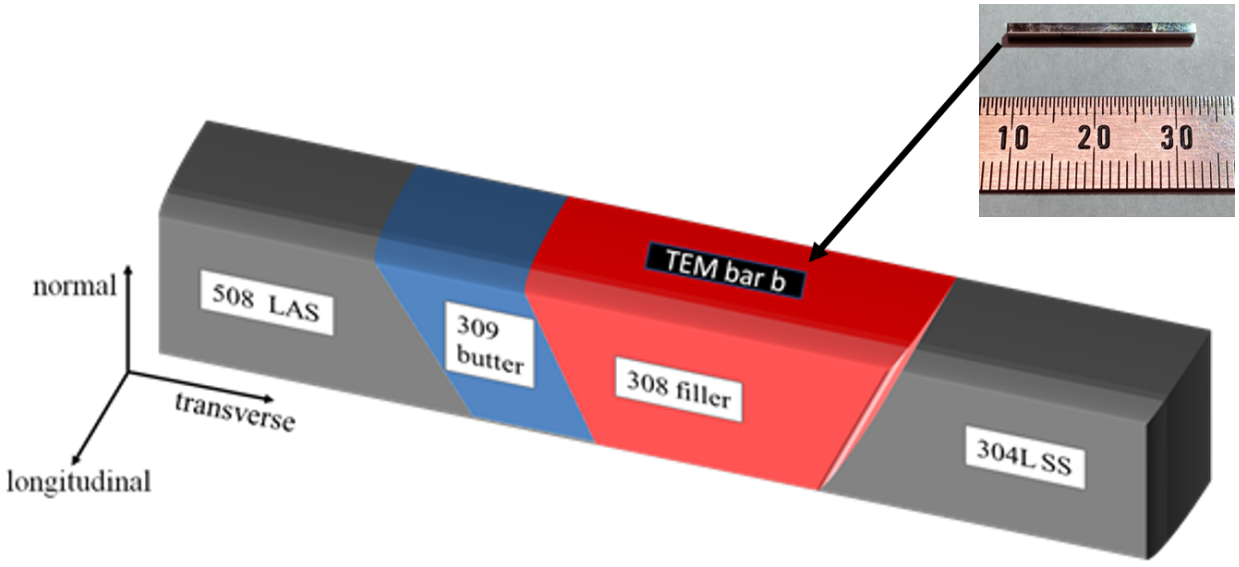

Figure 1. Schematic illustration of the SA508-309L-308L-304L weldment studied here. Inset: Irradiated TEM bar b.

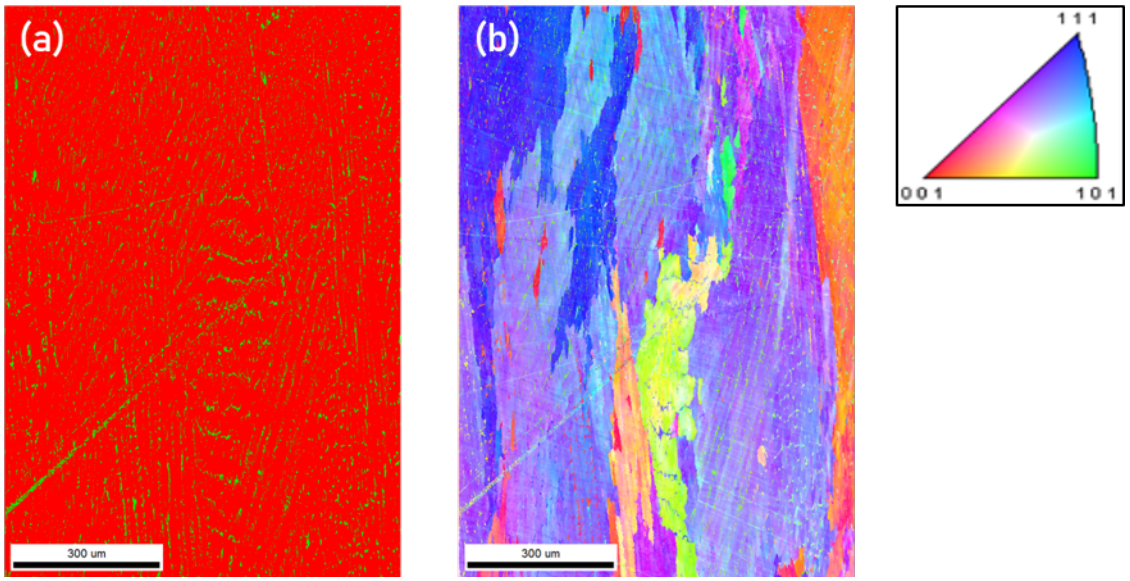

Figure 2. (a) EBSD phase map of the 308L filler weld joint, (b) EBSD orientation map of 308L filler weld joint.

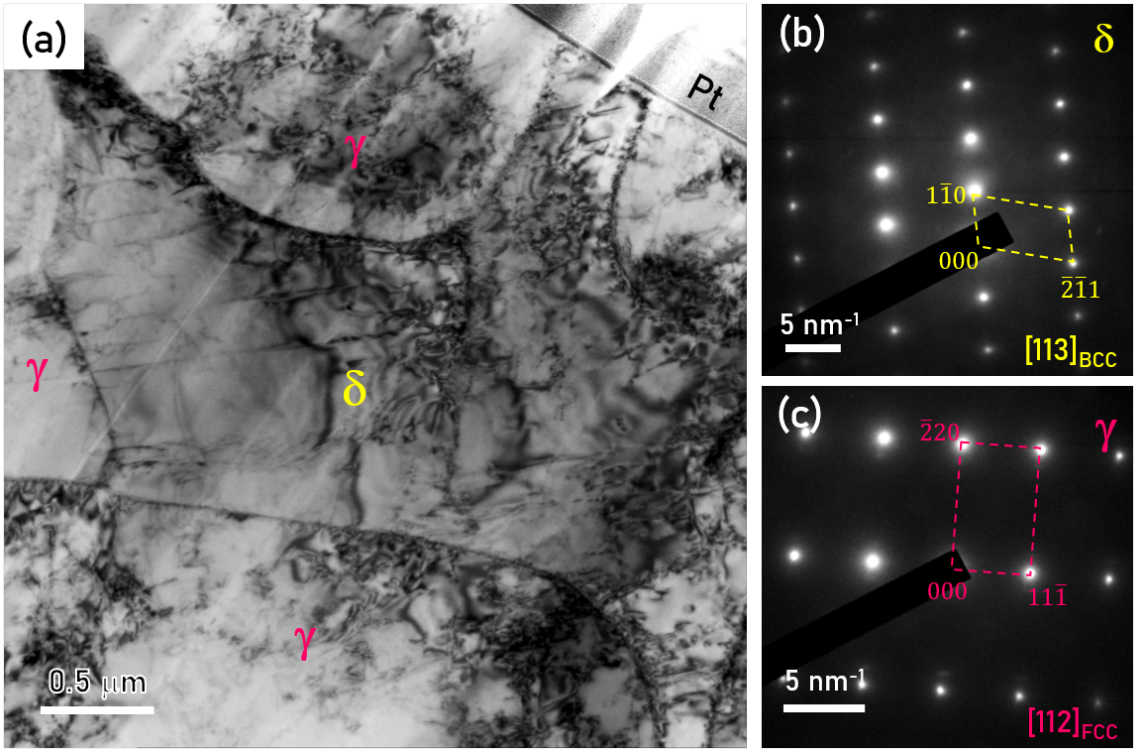

Figure 3. (a) Bright field TEM micrograph of 308L filler, (b) SAD pattern of δ ferrite, (c) SAD pattern of γ austenite.

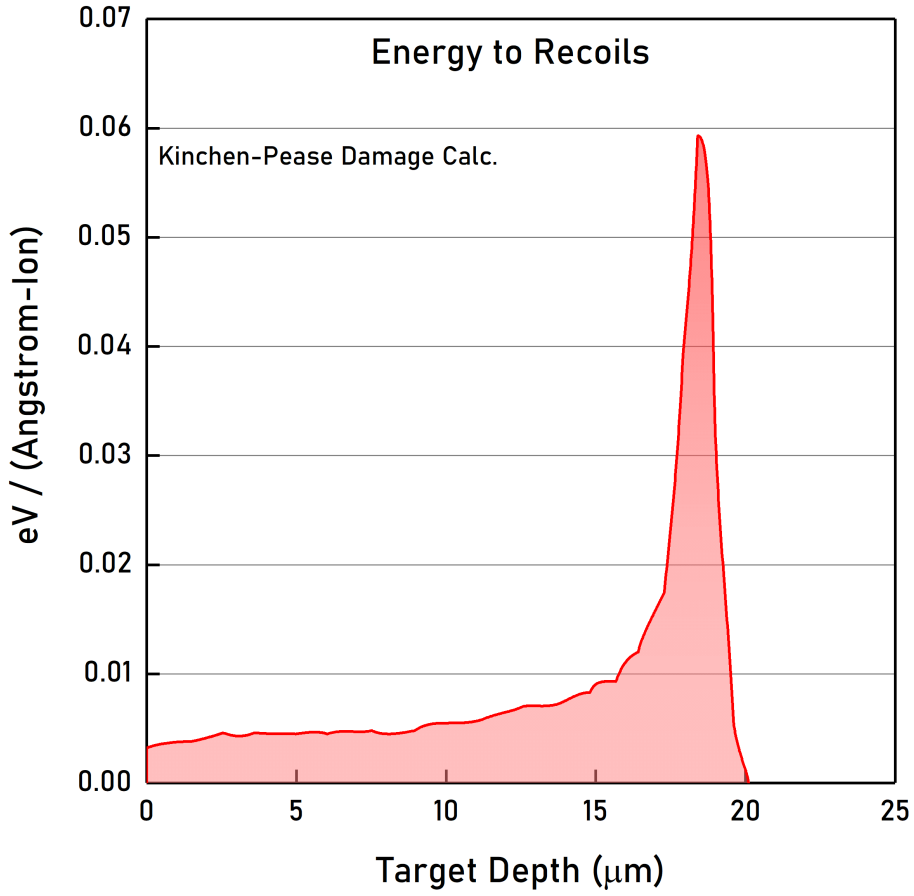

Figure 4. Simulated differential energy to recoils from proton irradiation in 308L (2 MeV protons at 360 ˚C and to damage level of 5 displacements per atom), which is calculated with the quick Kinchen-Pease option in TRIM.

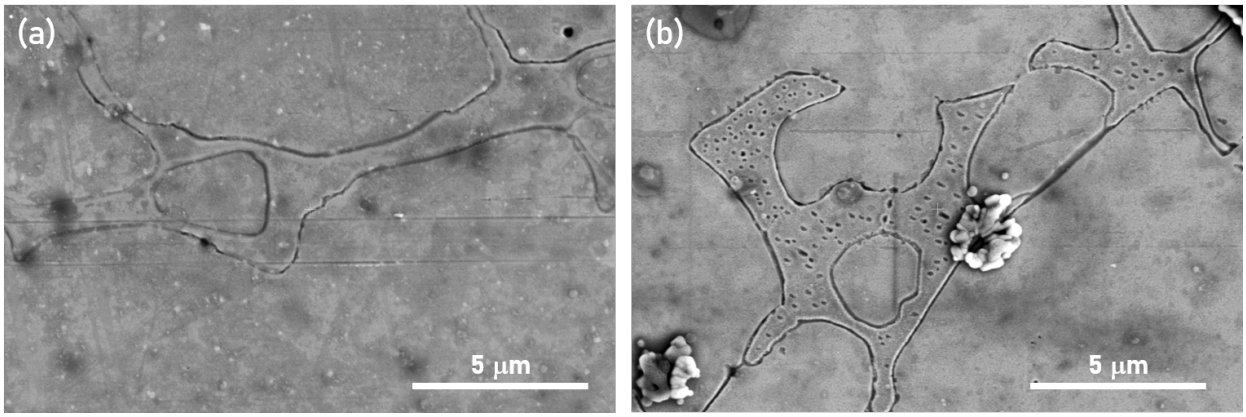

Figure 5. (a) SEM micrograph of unirradiated area of proton irradiated 308L filler: no precipitates are seen in either δ ferrite and austenite. (b) SEM micrograph of irradiated area of 308L filler: black dots are proton irradiation induced precipitates embedded in δ ferrite and intergranular precipitation is also observed. The white flower-like features are surface contaminants.

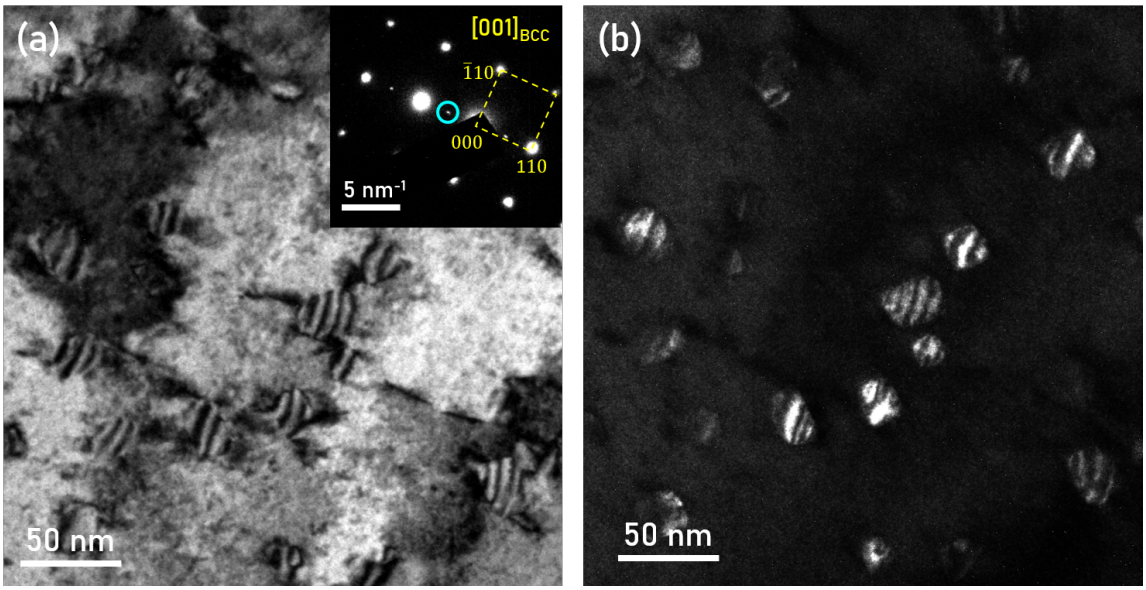

Figure 6. (a) TEM bright field micrograph indicated precipitates in proton irradiated δ ferrite; inset: diffraction pattern of δ ferrite along zone axis [001]; an extra diffraction spot (circled) is seen. (b) Dark field image generated from the extra diffraction spot circled in the inset, dark and bright rings in the precipitates are Moire fringes.

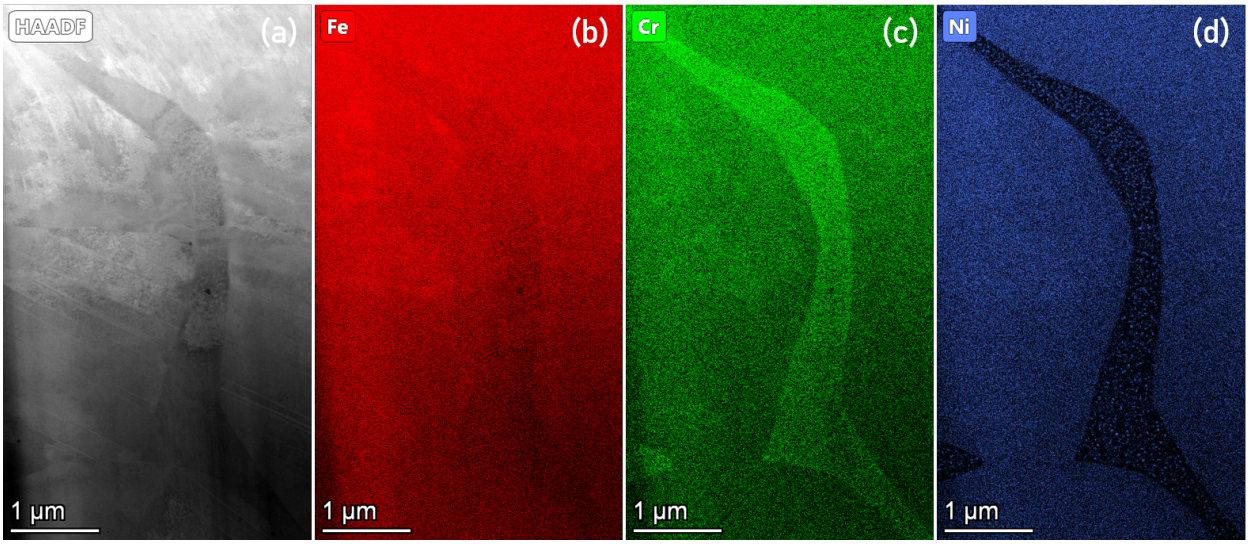

Figure 7. (a) STEM HAADF micrograph proton irradiated 308L filler material, the upper portion is close to the free surface. (b) STEM-EDS Fe map, (c) STEM-EDS Cr map, (d) STEM-EDS Ni map. Ni enriched dots (precipitates) are clearly seen in the δ ferrite grain running from the upper left, down through the center of the micrograph, to the lower right.

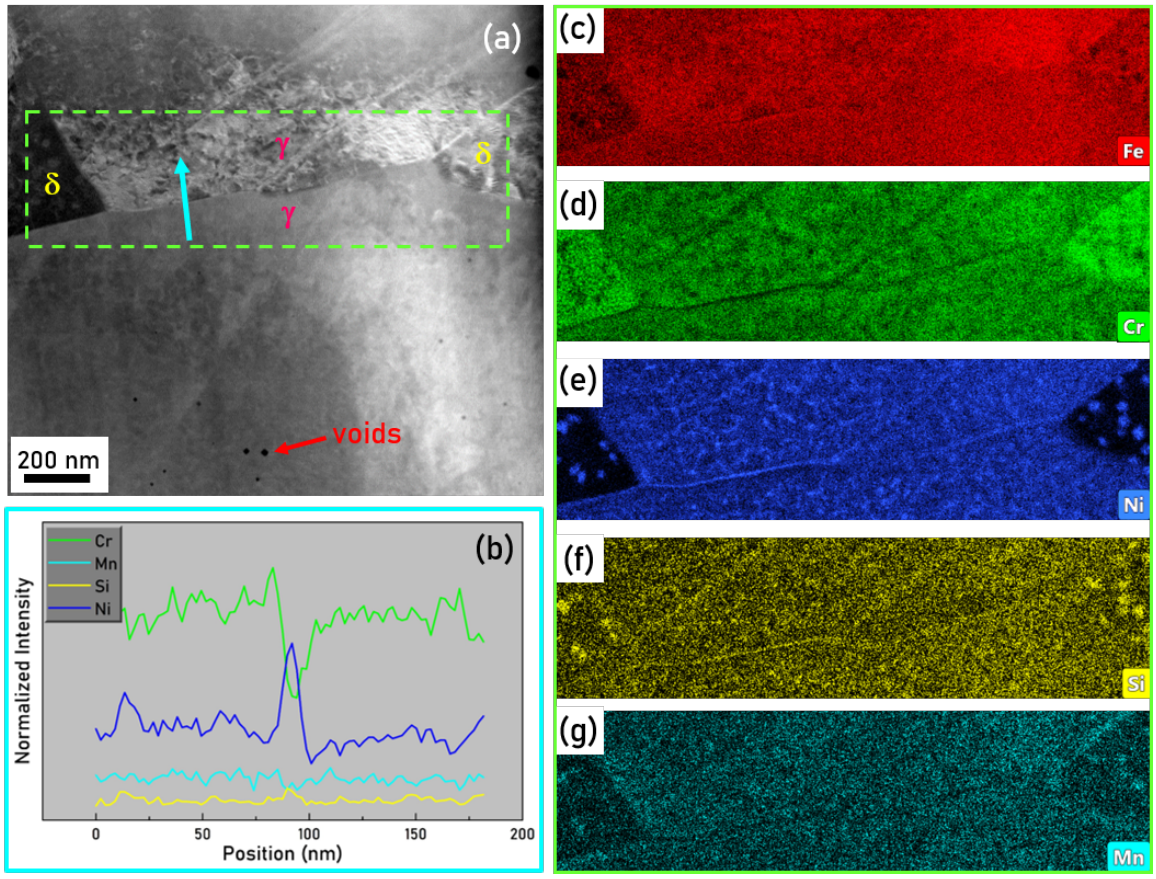

Figure 8. (a) HAADF image of proton irradiated 308L filler showing several phase boundaries at a depth of approximately 10 μm, (b) STEM-EDS line scan profile, (c) STEM-EDS Fe map, (d) STEM-EDS Cr map, (e) STEM-EDS Ni map, (f) STEM-EDS Si map, (g) STEM-EDS Mn map. The elemental maps are from the rectangular box in Figure 8a. The line scan in Figure 8b is along the upward arrow in Figure 8a. Voids that formed in γ austenite are identified in Figure 8a.

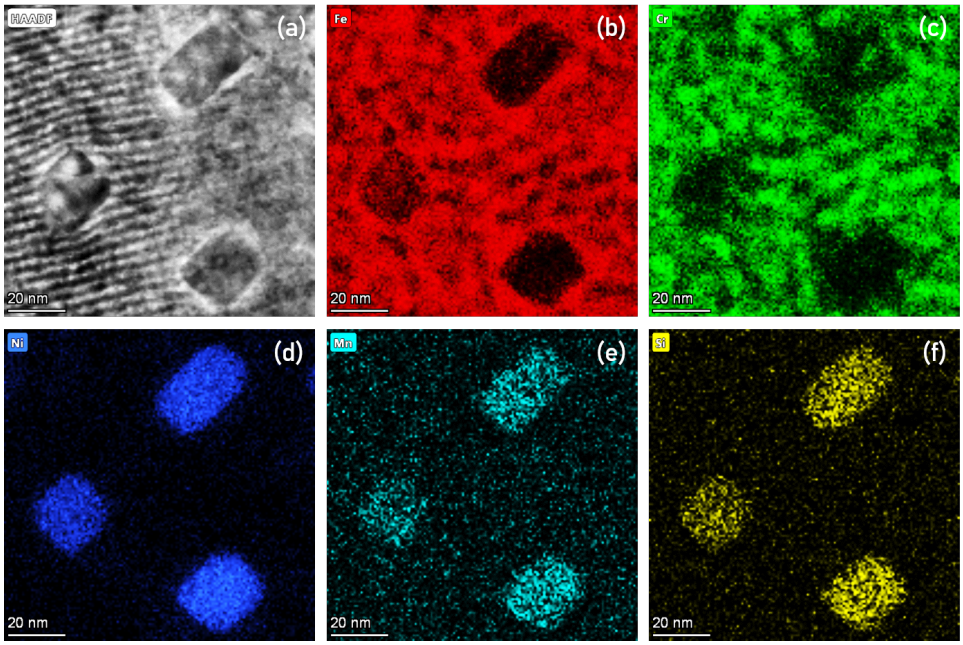

Figure 9. (a) HAADF image of δ ferrite with cuboid G phase precipitates at a depth 10 micrometers below the free surface. The fringes are resolved lattice planes of δ ferrite, (b) STEM-EDS Fe map, (c) STEM-EDS Cr map, (d) STEM-EDS Ni map, (e) STEM-EDS Mn map, (f) STEM-EDS Si map.

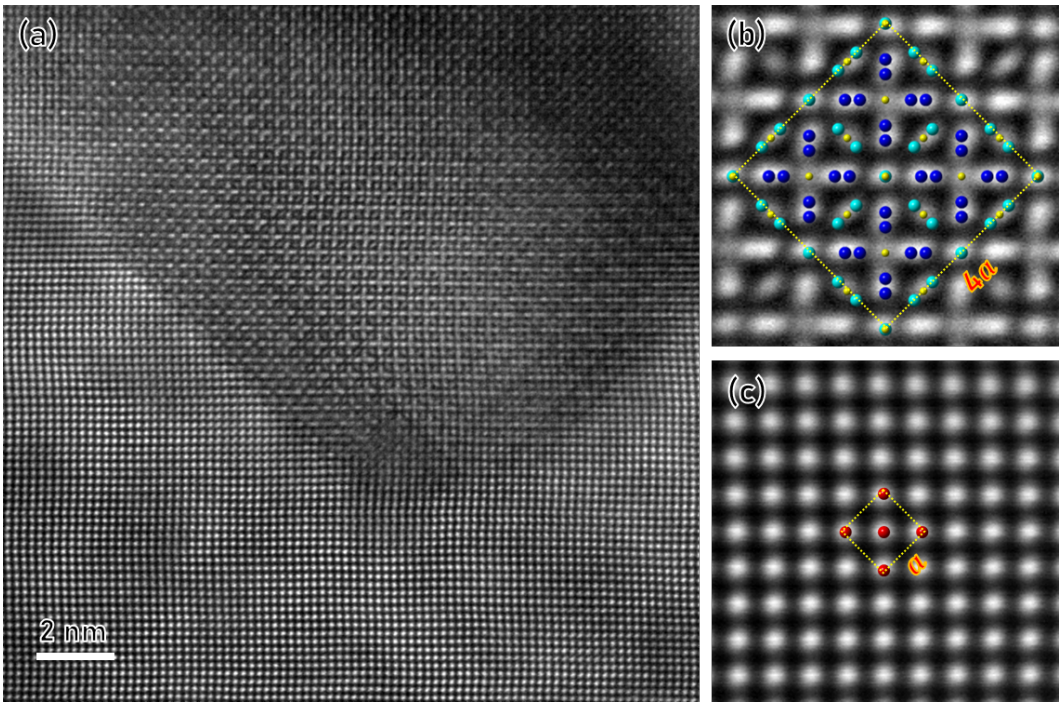

Figure. 10. (a) STEM HR micrograph of G-phase precipitates in proton irradiated δ ferrite from the 308L filler material, (b) lattice structure of G-phase precipitate at higher magnification with an overlay of Ni (blue), Si (yellow), and Mn (cyan) G-phase, (c) lattice structure of δ ferrite at higher magnification with an overlay of Fe (red). The zone axis for Figures 9b and c is [001].

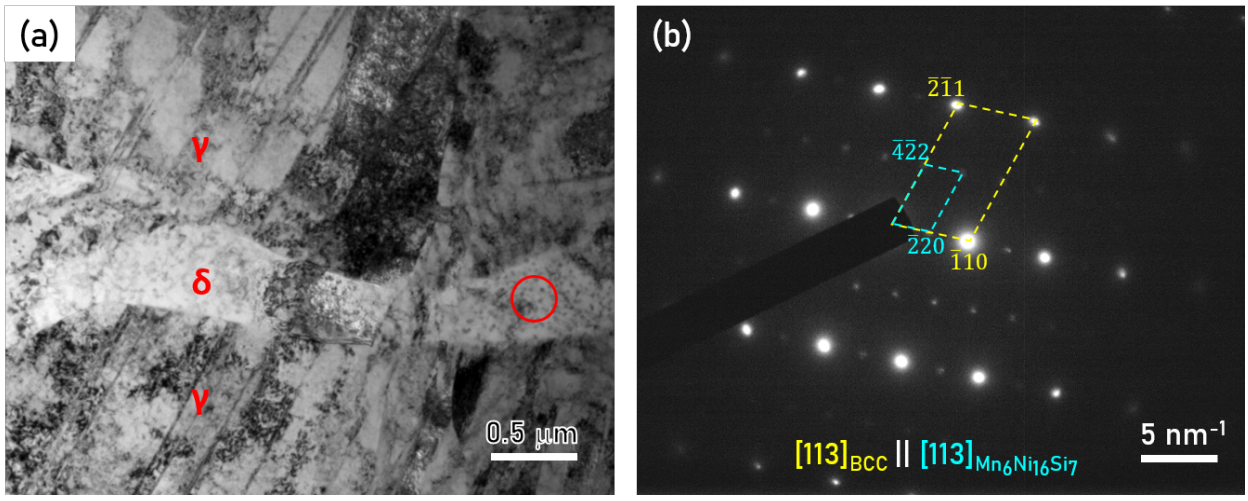

Figure 11. (a) Bright field TEM micrograph of proton irradiated 308L filler material with ferrite and austenite grains labeled. Black dots are G-phase precipitates in δ ferrite. Twinning is observed in the austenite grains, (b) selected area diffraction pattern from δ ferrite and G-phase $Mn_6Ni_{16}Si_7$ precipitates: yellow dotted box is the diffraction pattern of δ ferrite and cyan dotted box is the diffraction pattern of G-phase. The red circle in (a) is the SAD region for (b).

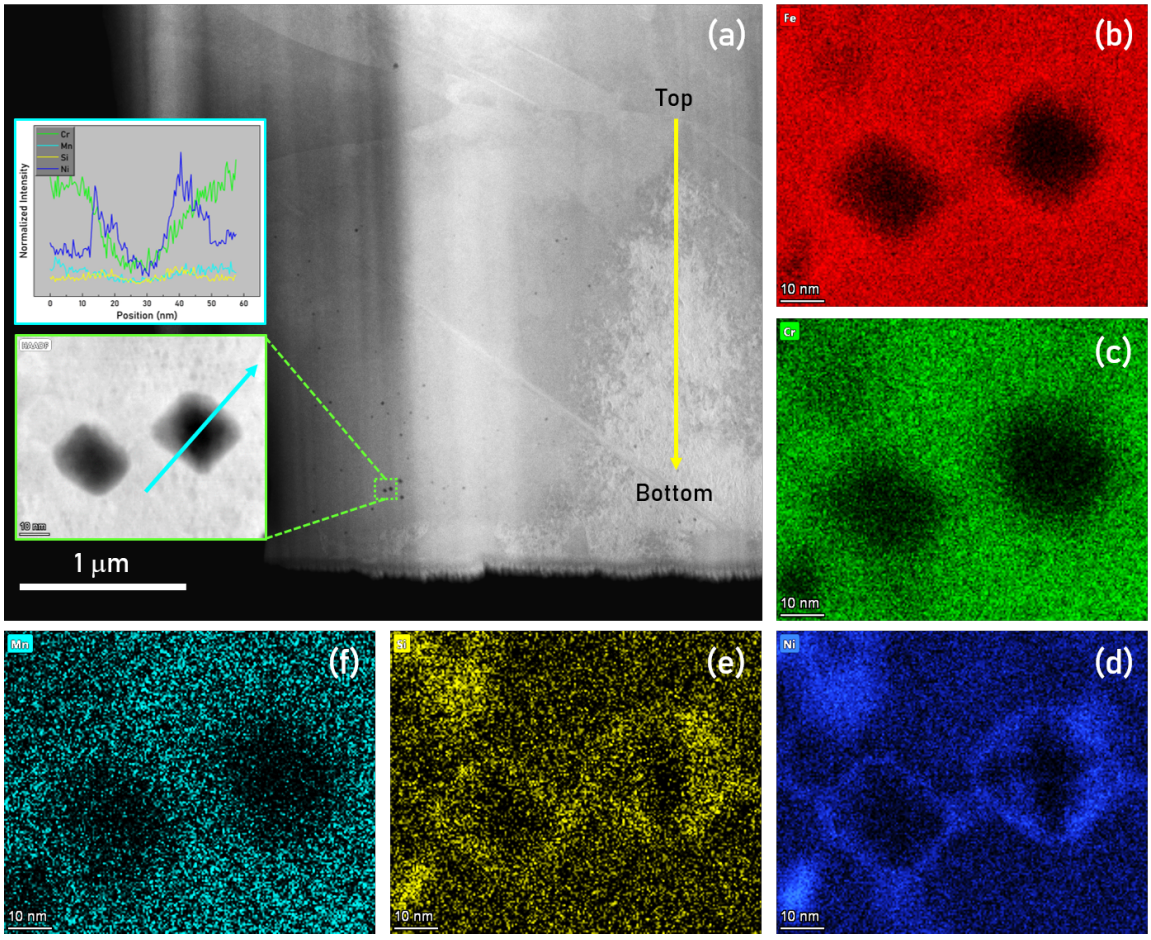

Figure 12. (a) HAADF image of a proton irradiated γ austenite grain exhibiting voids at a depth of approximately 10 μm; inset is a STEM-EDS line scan profile cross void as shown, (b) STEM-EDS Fe map, (c) STEM-EDS Cr map, (d) STEM-EDS Ni map, (e) STEM-EDS Si map, (f) STEM-EDS Mn map. The Ni and Si maps indicate an enrichment at void boundary.

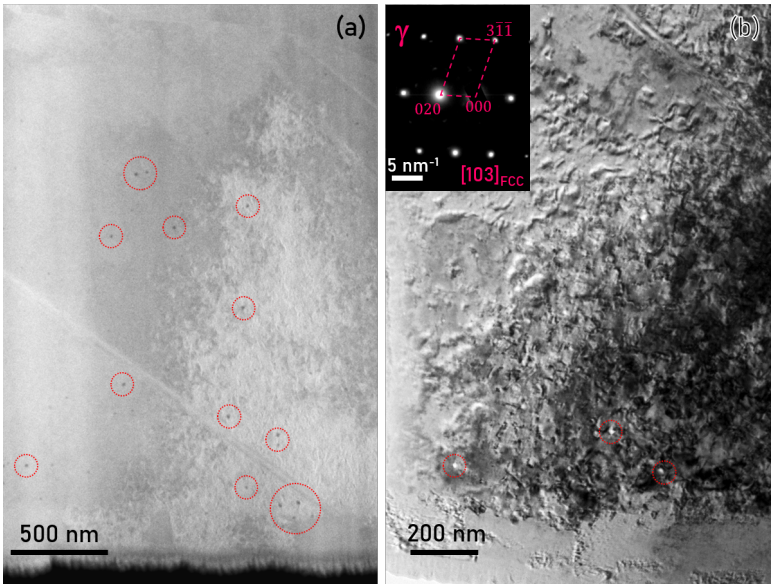

Figure 13. (a) Voids (circled) are imaged as dark spots in a STEM HAADF micrograph of proton irradiated γ austenite at a depth of approximately 10 μm, (b) Voids (circled) in a TEM bright field micrograph of the proton irradiated γ austenite; inset is a selected area diffraction pattern from a region containing both irradiated γ austenite and voids. Only a single diffraction pattern corresponding to γ austenite is observed, consistent with the circle features being voids as opposed to a second phase.

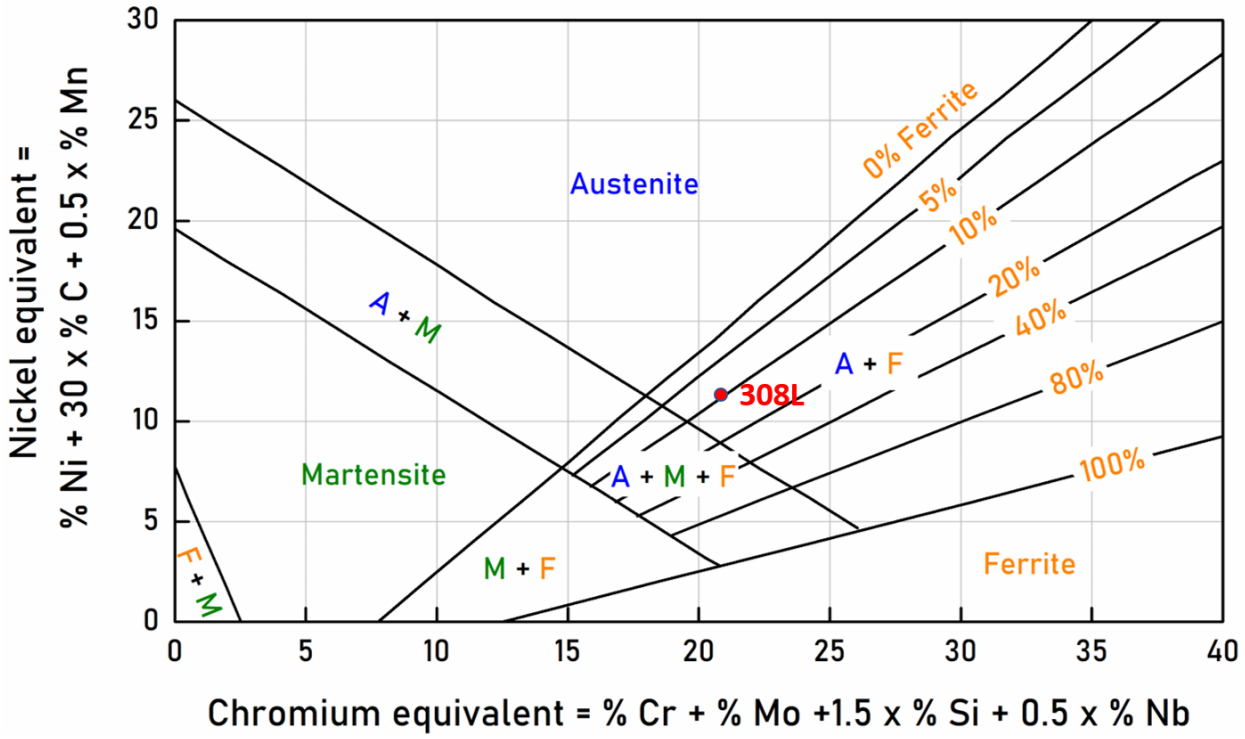

Figure 14. Schaeffler diagram for predicting δ-ferrite precipitate percentage in stainless steels [32, 33]. The equivalent Ni and Cr composition for our 308L filler material is as shown (red dot).

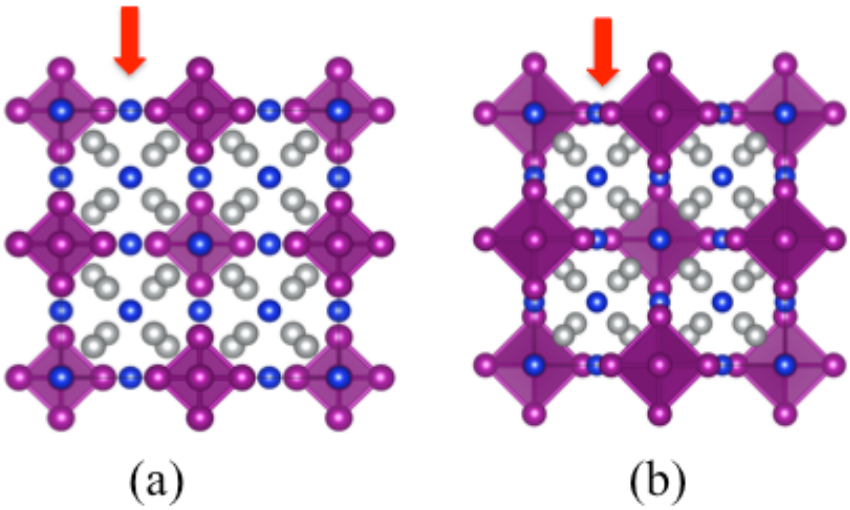

Figure 15. Relaxed crystal structures of $Mn_6Ni_{16}Si_7$ G phase for two different magnetic states. (a) Non-magnetic and (b) Ferromagnetic. Purple spheres – Mn atoms; Blue spheres – Si atoms; Grey spheres – Ni atoms. The arrows indicate the discrepancy between two relaxed structures.

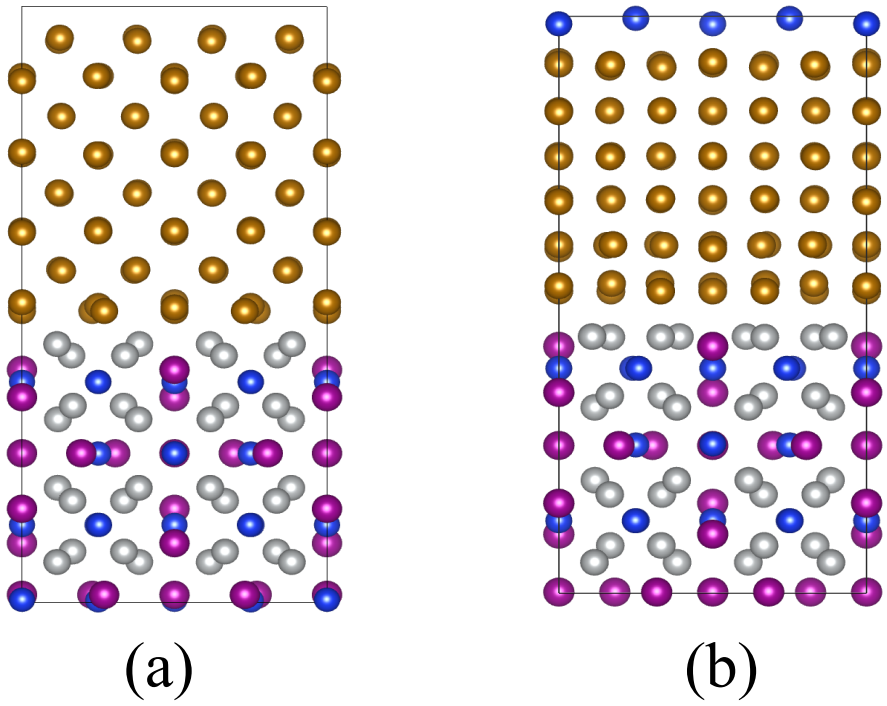

Figure 16. Relaxed interface structures of a) G phase + BCC Fe and b) G phase + FCC Fe. In both cases, the G phase is ferromagnetic and the Fe phases are approximately paramagnetic upon relaxation. Periodic boundary conditions are used so that some atoms wrap back between top and bottom of the system in (b). Yellow spheres: Fe atoms; Purple spheres – Mn atoms; Blue spheres – Si atoms; Grey spheres – Ni atoms.

9. Tables

Table 1. Specifications of SA508-304L DMW provided by ERPI.

Materials (at.%)	Cr	Ni	Mn	Mo	C	Cu	N	P	Si	Fe
SA508	0.18	0.76	1.38	0.47	1.01	0.08	NA	0.02	0.45	95.64
309L	24.38	12.80	1.60	0.04	0.05	0.09	NA	0.04	0.93	60.08
308L	21.07	9.69	1.99	0.09	0.07	0.24	NA	0.04	1.02	65.78
304L	19.23	7.53	1.73	0.19	0.09	0.38	0.27	0.05	0.55	69.96

Table 2. Lattice parameters of pure BCC Fe, pure FCC Fe, δ ferrite, γ austenite, and G-phase observed and simulated in this study.

Phase	BCC Fe	δ ferrite	δ this study/TEM	δ this study/DFT
a (nm)	0.286 [35]	0.286 [28]	0.283	0.283
Phase	FCC Fe	γ austenite	γ this study/TEM	γ this study/DFT
a (nm)	0.356 [36]	0.361 [29]	0.353	0.349
Phase		G-phase	G-phase this study/TEM	G-phase this study/DFT
a (nm)		1.109 [37]	1.072	1.110

Table 3. Composition of δ ferrite and γ austenite in unirradiated 308L from STEM-EDS.

Phase (at.%)	Cr	Fe	Ni	Si	Mn
δ ferrite	30.17	64.61	3.51	0.78	0.93
γ austenite	20.44	68.29	9.38	0.49	1.40

Table 4. DFT results of BCC Fe and FCC Fe of different magnetic states. The systems highlighted in bold are relevant to the three Fe phases (α, γ, δ) in observed in the equilibrium phase diagram.

Fe structure and magnetic state	**Fe phase**	**a_0 (Å)**	**Energy relative to α phase (eV/atom)**
BCC-FM (ground state)	**α (FM)**	**2.83 (Exp: ~2.86 [35])**	**0**
BCC-NM	δ (NM)	2.76	0.472
BCC-PM	**δ (PM)**	**2.83 (Exp: 2.83, this work)**	**0.169**
FCC-NM	γ (NM)	3.45	0.160
FCC-FM	γ (FM)	3.63	0.152
FCC-PM	**γ (PM)**	**3.49 (Exp: 3.53, this work)**	**0.133**

Table 5. DFT results of interfacial energies for the six combinations of FCC Fe, BCC Fe, and the G phase of different magnetic states. The systems highlighted in bold are relevant to the three Fe phases (α, γ, δ).

Initial magnetic state	**Final magnetic state**	**Represented Fe Phase**	**Interface energy (J/m^2)**
Both NM	BCC + G, NM	δ (NM)	-1.06
	FCC + G, NM	γ (NM)	1.14
Both FM	**BCC + G, FM**	**α (FM)**	**0.68**
	FCC + G, FM	γ (FM)	0.84
NM Fe + FM G	**PM BCC + FM G**	**δ (PM)**	-2.22 (Ref: NM BCC Fe, lower limit) **0.35 (Ref: PM BCC Fe)** 0.66 (Ref: PM FCC Fe, upper limit)
	PM FCC + FM G	**γ (PM)**	1.05 (Ref: NM FCC Fe) **1.25 (Ref: PM FCC Fe)**